DEUTSCHES ELEKTRONEN-SYNCHROTRON

DESY 94-137
MPI-Phe/94-20
August 1994

Physics from the First Year of H1 at HERA

C. Kiesling

Max-Planck-Institut für Physik, München

Representing the H1 Collaboration

ISSN 0418-9833

NOTKESTRASSE 85 - 22603 HAMBURG

To be sure that your preprints are promptly included in the
HIGH ENERGY PHYSICS INDEX,
send them to (if possible by air mail):

DESY **Bibliothek** **Notkestraße 85** **22603 Hamburg** **Germany**	**DESY-IfH** **Bibliothek** **Platanenallee 6** **15738 Zeuthen** **Germany**

DESY 94-137
MPI-Phe/94-20
August 1994

ISSN 0418-9833

PHYSICS FROM THE FIRST YEAR OF H1 AT HERA

Christian Kiesling
Max-Planck-Institut für Physik
80805 München, Germany

Representing the H1 Collaboration *

ABSTRACT

In this report we summarize the results from the H1 experiment at HERA, using the data from the first year of running, 1992, where an integrated luminosity of 25 nb^{-1} has been recorded. These results include photoproduction, the measurement of the deep inelastic scattering, both for neutral current reactions, and the search for physics beyond the standard model. Apart from the measurement of a moderate rise in the total photoproduction cross section, clear evidence is seen for hard interactions in single particle spectra and jet production, requiring a "resolved" photon as expected in QCD. The investigation of the global properties of hadronic final states in deep inelastic scattering demonstrates the need for further improvement of present QCD models. Evidence is found for a class of events with diffractive characteristics, exhibiting a large gap of hadronic energy flow about the proton direction. The proton structure function $F_2^p(x, Q^2)$ has been measured for neutral current events for Bjorken x in the range $10^{-4} - 10^{-2}$ and $Q^2 > 5$ GeV^2, showing a steep rise towards small x. Furthermore, using 1993 data, a measurement of the cross section for charged current events is presented, clearly demonstrating, for the first time, the propagator effect of the W boson. Finally, new limits on leptoquarks, leptogluons, and excited electrons have been determined.

*Invited talk at the XXI Summer Institute on Particle Physics, Spin Structure in High Energy Processes, SLAC, Stanford, California 94309, July 26 - August 6, 1993

1 Introduction

With the turn-on of HERA in May 1992, the longstanding tradition of deep inelastic scattering of leptons on nuclear targets, starting roughly 25 years ago with the celebrated experiments at SLAC,[1] is being continued into a new kinematic domain. Deep inelastic scattering experiments (for results from recent fixed-target experiments see[2,3]) have paved the way towards our present understanding of the structure of the nucleon and the nature of interactions between quarks and leptons.

HERA collides electrons of 26.7 GeV on 820 GeV protons, providing a center-of-mass energy of 296 GeV, and thus extends the accessible range of center of mass energy and momentum transfer by more than an order of magnitude: HERA pushes into yet unexplored kinematical regions, down to values of the Bjorken x below 10^{-4} and up to large four-momentum transfer squared Q^2, exceeding 10^4 GeV^2.

The HERA collider[4] consists of two independent accelerators and is designed to accelerate and store, respectively, 820 GeV protons and 30 GeV electrons, and to collide the two counterrotating beams head-on in four interaction points arranged symmetrically around its circumference of 6.3 km. While the superconducting proton ring has reached its design energy, the electron ring is presently operated at 26.7 GeV. The particles in the accelerators are grouped in bunches, separated by 96 ns in arrival time at the interaction points. In the first year of running (1992) ten proton and ten electron bunches were injected, where one bunch for each beam was left without a colliding partner in the interaction regions ("pilot bunch"). In 1993 the number of bunches was increased to 90, with typical beam currents of 10-15 mA for each particle type. The final number of bunches will be 210, corresponding to 60 and 160 mA for the electron and proton currents, respectively, providing an instantaneous luminosity of 1.5×10^{31} cm^{-2}s^{-1}.

One of the important physics goals at HERA will be the measurement of the structure functions which have been recognized as powerful sources of information on the substructure of matter. This physics program continues the "classical" field of nuclear form factors[5] into the sub-Fermi scale: At HERA, due to the very high energies accessible, the extended range of four-momentum transfer Q^2 will allow probing nucleon matter down to spatial distances of about 10^{-18} cm. These data will provide important constraints to the present theory of strong interac-

tions, Quantum Chromodynamics (QCD). In addition, the study of hadronic final states in deep inelastic scattering events, e. g. single particle distributions or jet production, enables detailed comparisons with QCD models. The signature of hadronic final states is also indicative of particular production mechanisms, such as diffractive production, which is expected to occur also in deep inelastic scattering.[6,7]

Furthermore, the high center-of-mass energy at HERA will allow, for the first time, probing proton constituents which carry a very small share of the total momentum: At Bjorken $x \sim 10^{-5}$ and below, the model of quasi-free, noninteracting partons is bound to fail[8]: If the structure function rises with decreasing x as anticipated, producing more and more partons (quarks and gluons) at small x, the cross section will eventually conflict with unitarity limits. This may be cured allowing for "screening" effects, i. e. nonlinear interactions between quarks and gluons, leading to saturation[8-10] of the structure function at very small x. These effects are unimportant at large x, where the parton densities are lower.

Besides the low x physics, the low Q^2 region also offers a rich physics potential[11]: The central issue of low Q^2 investigations at HERA is the photon, the nature of which can be probed in a new kinematical regime. In this regime quantum fluctuations become important; transforming the photon into a quark-antiquark pair or an even more complex partonic system, which in turn interacts with the partons of the proton. Measurements of hadron production from quasi-real photons on protons at HERA are expected to provide new insight into the partonic contents of the photon, most importantly its gluon component. Photoproduction reactions should also complement the measurements of the proton structure function, where heavy quark and J/ψ production will help to extract the gluon distribution inside the proton.

Another interesting aspect of HERA is the possiblity to measure electroweak processes.[12] While the neutral current (NC) reactions are dominated by photon exchange due to the propagator term $1/(Q^2 + M^2)$ (M is the mass of the exchanged gauge boson, γ or Z^0) over most of the Q^2 range ($< 10^4$ GeV^2) the charged current (CC) process involves only weak boson (W) exchange. Since the HERA center-of-mass energy is around the Fermi scale, corresponding to an equivalent laboratory beam energy on a stationary proton target of roughly 50 TeV, substantial deviation of the cross section from linearity (infinite W mass) is expected. With the standard W exchange, the total cross section for CC events

is suppressed by about a factor of 3 with respect to the linear extrapolation. This means that even with a modest number of CC events this dramatic effect will be visible.

Finally, any new accelerator exploring a new energy regime, has the exciting prospect to look for new physics. This program is carried out either by direct searches for exotic particles with masses below the available center-of-mass energy, or by searching for signals of new physics at much higher mass scales manifesting themselves in a more subtle way, however, as deviations (propagator effects) from the standard expectations. While the latter investigations usually require high luminosity, direct searches are meaningful even with modest statistics. Given its high center-of-mass energy and unique inital states (electron and quarks or gluons) HERA offers the exciting possiblity to search for leptoquarks, leptogluons and excited leptons or quarks, which are demanded in many models of unified strong and electroweak interactions and various models of lepton/quark compositeness.[13]

This report is structured as follows: Working our way up from very low Q^2 we describe, after the presentation of the HERA kinematics and a description of the H1 detector, the results on photoproduction, most importantly the measurement of the total cross section, evidence for hard scattering and for the partonic nature of the photon (" resolved photon") and, in particular, its gluon content. The deep inelastic scattering (NC) is discussed in section 5, presenting the measurements of the proton structure function $F_2^p(x, Q^2)$ in the kinematic range $5 < Q^2 < 100$ GeV^2 and $10^{-4} < x < 10^{-2}$. Furthermore studies of the hadronic final state and a first measurement of the gluon structure function $G(x, Q^2)$ are presented. A special class of deep inelastic events with a large rapidity gap with respect to the proton remnants is discussed in section 5.5. From an analysis of CC events (section 5.6) a first measurement of the CC cross section is derived, clearly demonstrating the W propagator effect. Section 6 finally presents the results from searches for new particles. Most of the results given in this report are based on 1992 data with an integrated luminosity of 25 nb^{-1} , which have been already reported at several conferences[14,15] and publications (see below, and also[16]). Some recently completed analyses on the 1993 data (CC cross section and leptoquark search), corresponding to about 350 nb^{-1} , are also included. These data, however, were not discussed at the 1993 Summer Institute.

2 Kinematics

The kinematics of the inclusive deep inelastic scattering process $ep \to e(\nu)X$ at fixed center-of-mass energy, $\sqrt{s}$, is determined by two independent variables, conventionally chosen from Q^2 and the scaling quantities x and y. Q^2 is the four-momentum transfer squared between the ingoing and outgoing lepton, x in the naive quark parton model (QPM) is the momentum fraction of the proton carried by the struck parton (Bjorken x), and y is the fraction of the energy transferred from the initial electron to the hadronic system. The lowest order diagram for this process is depicted in fig. 1 and defines the four-vectors involved in the kinematics. Since the H1 experiment at HERA (see below) measures both the scattered electron and the hadronic final state produced between the struck parton and the proton remnant, the collision kinematics can be determined from electron variables, hadronic variables or a mixture of both.

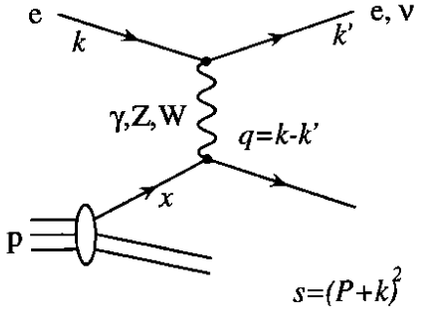

Figure 1: *Born term diagram for deep inelastic scattering*

In Lorentz-invariant notation the kinematical variables are defined as follows:

$$Q^2 = -q^2 = -(k - k')^2 \tag{1}$$

$$y = \frac{P \cdot q}{P \cdot k} \tag{2}$$

$$x = \frac{Q^2}{2P \cdot q} \tag{3}$$

Neglecting the proton mass M, the invariant mass squared W^2 of the hadronic final state, in terms of the variables defined in eqs. (1-3), is given by

$$W^2 = (q + P)^2 = Q^2 \frac{1 - x}{x} \tag{4}$$

At HERA the center-of-mass energy squared, neglecting the mass of the proton, is defined as

$$s = (k + P)^2 = 4EE_p \tag{5}$$

where E and E_p are the energies of the incoming electron and proton, respectively. With the present HERA beam energies s reaches 87600 GeV^2. Due to this high center-of-mass energy, using

$$Q^2 = xys, \tag{6}$$

from eqns. (1-3), x values down to $\sim 10^{-4}$ in the deep inelastic regime ($Q^2 > 10$ GeV^2) can be accessed at HERA.

The kinematic variables in charged-lepton nucleon scattering are traditionally determined from the polar angle θ and the energy E' of the scattered lepton through the relations

$$Q^2 = 4EE' \cos^2\left(\frac{\theta}{2}\right), \tag{7}$$

$$y = 1 - \frac{E'}{E} \sin^2\left(\frac{\theta}{2}\right) \tag{8}$$

and the Bjorken variable x is calculated using eqn. (6):

$$x = \frac{Q^2}{sy} \tag{9}$$

Polar angles, such as θ, are measured relative to the proton beam direction, termed the "forward direction" (corresponding to $\theta = 0$ throughout this report). The kinematics for the scattered electron in the (x, Q^2) plane is shown in fig. 2. One notices that for a large region in the (x, Q^2) plane, corresponding roughly to $y < 0.1$, the energy of the scattered electron is close to the incident electron beam energy. This leads to a peak in the electron energy spectrum, termed the "kinematic peak", which serves beneficially for calibration purposes (see below).

The bulk of data for the deep inelastic scattering events are expected at low Q^2 and low x, due to the $1/(Q^4 x)$ dependence of the cross section (eqn. (16). The resolution in Q^2, when determined according to eqn. (7), is dominated by the electron energy resolution. In H1, the determination of Q^2 using the scattered electron is superior to others based on the hadronic energy or angle measurement. This is not true for the variable y, which from the scattered electron alone cannot be accurately determined below $y \leq 0.05$, as the resolution of such a determination varies like $1/y$, as can easily be seen differentiating eqn. (8).

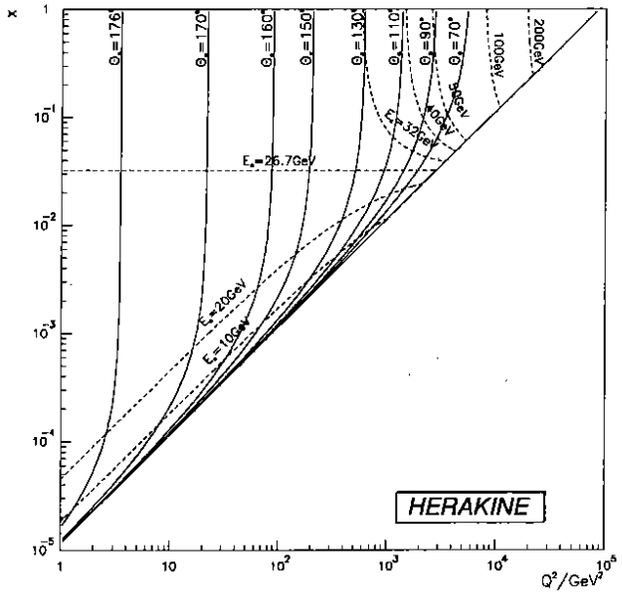

Figure 2: *Lines of constant energy and scattering angle for the scattered electron in the (x, Q^2) plane for deep inelastic scattering events.*

In a second method of determining the kinematics y is defined with the help of the hadronic final state, which allows accessing the lower y or larger x region. The hadronic y variable is determined using the relation[17]

$$y_h = \frac{1}{2E} \sum_{hadrons} (E_h - p_{z,h}) \tag{10}$$

$$Q^2_h = \frac{1}{1 - y_h} \sum_{hadrons} (p_{T,h})^2 \tag{11}$$

where E_h is the energy of a hadron and $p_{z,h}$ ($p_{T,h}$) its momentum component along (transverse) to the $+z$ (proton beam) direction.

Photoproduction processes are studied by measuring neutral current reactions for which the electron is scattered into the backward ($\theta = 180^0$) direction with $Q^2 \sim 0$. For these reactions the variable y reduces to the energy of the incident quasi-real photon, measured in units of the electron beam energy:

$$y = E_\gamma = 1 - \frac{E'}{E} \tag{12}$$

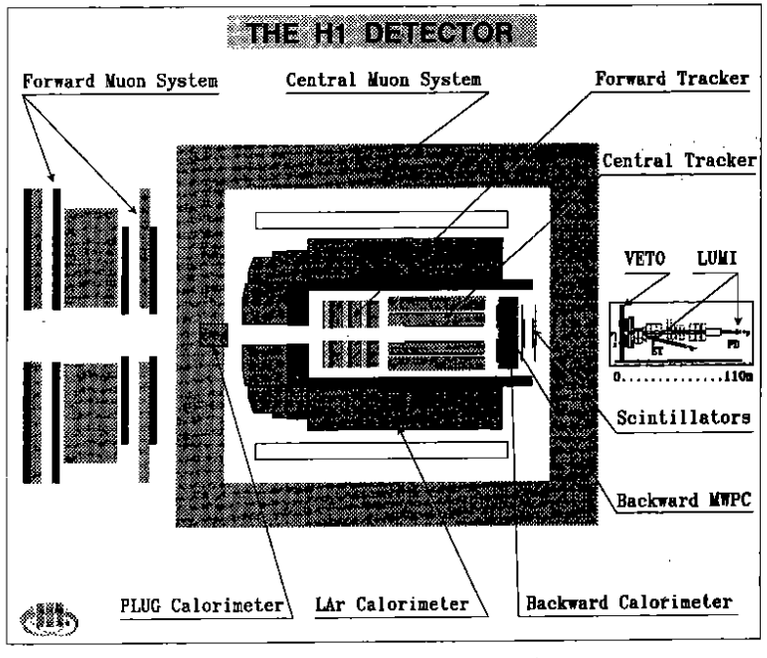

Figure 3: *Schematic view of the H1 detector*

3 The H1 Detector

The H1 detector is one of the two large general purpose detectors at HERA, following the design principles of most modern collider experiments: It provides almost hermetic (4π coverage) hadronic energy flow measurement, charged particle reconstruction and precise lepton (electron and muon) identification and measurement. Only 5 years after submission of the technical proposal in 1986, the H1 detector went into operation in the HERA North Hall in spring 1991, where a substantial program of debugging with cosmic ray data was carried out until the first arrival of luminosity on May 31, 1992.

Figure 3 shows a schematic overview, cut along the beam axis, of the various components of the H1 detector. A notable distinction of the experiments at HERA with respect to other existing colliding beam detectors is the enhanced instrumentation in the forward (proton) direction due to the very asymmetric electron and proton beam energies, boosting the center-of-mass system (CMS) by a Lorentz-γ

factor of about 2.9. Starting the description of H1 from the center of the interaction region, the detector consists of a central tracker (CT), surrounded by a Liquid Argon (LAr) calorimeter, followed by a superconducting solenoid of 6 m diameter providing a magnetic field of 1.14 T with a uniformity of better than 2 % within the tracking volume, an instrumented flux return yoke, and large planar muon chambers. In somewhat more detail the H1 detector contains the following components (a full description of the H1 detector can be found elsewhere[18]):

- The central and forward tracking system: Each of the two mechanically distinct tracking detectors contains several layers of drift chambers interspersed with multiwire proportional chambers for triggering.

  The central tracking detector (CTD) covers the polar angular range $25^0 < \theta < 155^0$ and consists of two large concentric jet drift chamber modules (CJC1 and CJC2), with inner radii of 20.3 (53) cm and outer radii of 45.1 (84.4) cm, for CJC1 (CJC2). The total of 2640 sense wires are strung parallel to the beam direction and the drift cells are inclined by about 30^0 with respect to the radial direction.

  A space point resolution of 170 μm has been achieved in the drift coordinate ($r\phi$ plane). The z coordinate can be determined, by comparing the signals read out at both ends of the sense wire, with a precision of about 2 cm. From the signals recorded in these chambers the transverse particle momentum is determined with a precision of $\Delta p/p^2 \sim 0.009$ GeV^{-1} in the magnetic field provided by the superconducting solenoid. The double track resolution in the jet chambers is about 2 mm.

  Two thin drift chambers ("z-chambers" CIZ and COZ), sandwiching the inner jet chamber (CJC1), complement the precision measurement of charged particles in the barrel. For these chambers the sense wires are strung perpendicular (the drift direction is parallel) to the beam axis. The polar angles covered by inner (CIZ) z-chamber and the outer (COZ) z-chamber are $16^0 < \theta < 169^0$ and $25^0 < \theta < 156^0$, respectively. Each chamber delivers track elements with typically 300 μm resolution in z and about 2 % of 2π in the azimuthal angle ϕ.

  Inside of CIZ and outside of COZ two multiwire proportional chambers (CIP and COP) are mounted, each with a double layer of anode wires. Since their main purpose is triggering, a pad segmented cathode readout (480 pads for

CIP, 288 for COP) was chosen. The angular coverage of CIP (COP) is $10^0 < \theta < 170^0$ ($25^0 < \theta < 155^0$).

The forward tracking detector (FTD) accepts tracks between 6^0 and 25^0. It consists of three nearly identical supermodules. Each supermodule includes, increasing in z, three different orientations of planar drift chambers for accurate θ measurement, a multiwire proportional chamber for triggering, a passive transition radiator (see below), and a radial drift chamber for accurate $r\phi$ measurement and radius measurement by charge division readout. The resolutions achieved are 200 μm in the $r\phi$ plane (radial chambers) and 170 μm in the x and y coordinates (planar chambers).

In both the CTD and FTD drift chambers, measurement of the charge deposited on the sense wires enables particle identification by means of the specific energy loss dE/dx, where typical resolutions are about 10 %. In the forward direction, where high track densities and high momenta are expected, e/π discrimination is further enhanced by transition radiation detected in the radial drift chambers of the FTD. In combination with the liquid argon calorimeter (see below), excellent e/π discrimination ($< 10^{-3}$ hadron contamination) over a polar angular range $6^0 < \theta < 171^0$ can be achieved.

The backward region $155^0 < \theta < 175^0$ is covered by the backward multiwire proportional chamber (BPC), which has four different orientations of anode wire planes. The chamber serves for measuring the direction of particles. A space point given by the BPC contributes 0.5 mrad to the angular resolution, which is in the same order of magnitude as the multiple scattering in the material in front of the chamber.

- The liquid argon calorimeter (LAC): It surrounds the tracker and is optimized for precise measurements of electrons (photons) together with very good performance in the measurement of jets with high particle densities. These requirements are best met by segmenting the calorimeter into an electromagnetic part (EMC) and a hadronic part (HAC) and placing the entire calorimeter inside the magnet. In this way one minimizes both the amount of dead material in front of the electromagnetic calorimeter for optimal energy resolution and the overall size of the calorimeter. The LAC covers the polar angular range $4^0 < \theta < 153^0$.

The LAr calorimeter is segmented along the z direction in eight selfsupporting "wheels". One single large cryostat houses all the wheels. Each of the six barrel wheels is segmented in the azimuthal angle ϕ into eight identical octants ("stacks"). Each stack in turn is divided into an electromagnetic section (EMC) with lead as absorber material, starting at a radius of 86 cm, followed by a hadronic (HAC) section which has welded non-magnetic steel absorber plates. The plate orientations are such that the angle of incidence for particles originating from the interaction point is always larger than 45^0. Great care has been taken to minimize the cracks between the different stacks and wheels. All z cracks (boundaries between the different wheels) are perpendicular to the beam axis and in no case pointing to the interaction point (IP). While the EMC has ϕ cracks (boundaries between stacks within a wheel) pointing to IP, the boundaries of the subsequent hadronic sections are inclined in ϕ and therefore guarantee a hermetic calorimeter. The total thickness of the electromagnetic calorimeter varies between 20 to 30 radiation lenghts (X_0), the total depth of the calorimeter varies between 4.5 and 8 interaction lengths (λ), depending on the polar angle.

The gaps between the absorber plates are equipped with highly segmented readout structures. The granularity of the read-out cells is based on the requirement of good separation of electromagnetic and hadronic showers. The longitudinal segmentation is three to four-fold for the EMC and four to six-fold for the HAC. The transverse structure is realized in pads of size about 4 by 4 cm^2 for EMC and 8 by 8 cm^2 for HAC. A total of 45,000 readout channels result for the entire LAr calorimeter, out of which about 30,800 are situated in its electromagnetic part. Typical noise levels (white noise) in the readout channels are between 10 and 30 MeV, depending on the channel capacity.

For trigger purposes the calorimeter cells are summed into 656 projective trigger towers (TT), which are discriminated against individual thresholds to suppress white and coherent noise and are then summed to 240 so-called Big Towers (BT). The BT's are the building blocks of a digital trigger processor calculating various scalar and vector sums, such as the total transverse energy E_T or the total missing transverse energy E_{Tmiss}, which are then passed through programmable threshold functions.

An extensive calibration program with test beams at CERN[19] using the

different types of H1 calorimeter stacks has provided the basic calibration constants for the calorimeter. The energy resolution $\sigma(E)/E$ obtained for electrons was between 10 % and 13 $\%/\sqrt{E}$ (E in GeV) with a constant term below 1 %. Using software weighting techniques, which are based on the recognition of local electromagnetic energy deposition, a hadron resolution of about 50 $\%/\sqrt{E}$ has been obtained with a constant term below 2 %. These results have been basically confirmed at HERA using cosmics and deep inelastic scattering events. The absolute scales of the energy response at HERA have been verified with charged particles by comparing their momentum measured in the central tracker with the associated energy deposited in the calorimeter. With electrons and positrons produced by Bremsstrahlung from cosmic ray muons, the electromagnetic scale has been checked to ±3%. Using negatively charged particle tracks originating from the *ep* interaction region, the hadronic scale has been checked to ±10%. Furthermore, a study of the balance of transverse momentum between the scattered electron measured in the backward calorimeter and the recoiling hadronic system measured in the LAr calorimeter demonstrates that the overall hadronic energy scale is understood to within ±5%. Note that these numbers are limited presently only by the available statistics at HERA. Furthermore the long-term stability of the LAr calorimeter could be verified: Purity contol systems have shown that, since the calorimeter started operation in 1991, the signal attenuation per year was below 0.5 %.

- The backward electromagnetic calorimeter (BEMC): The backward ($-z$) region of the H1 detector is instrumented with a conventional electromagnetic lead-scintillator sandwich calorimeter. Its primary task is to measure energies and directions of electrons scattered under small angles from deep inelastic processes with moderate four-momentum transfer $Q^2 < 100$ GeV^2. BEMC, which covers the polar angular range $150^0 < \theta < 176^0$, consists of 88 stacks aligned parallel to the beam, each with a depth of 22 X_0, corresponding to about 1 λ, with quadratic cross section of 16 by 16 cm^2. Each stack is read out by four PIN photodiodes.

  Since BEMC has to operate in a very high rate environment caused by the illumination of the rear side with secondary hadrons from upstream interactions of the proton beam with residual gas in the beam pipe ("beam-gas") or with machine components ("beam-wall"), fast energy signals of 100 ns

rise time are formed for triggering. Typical thresholds for electromagnetic clusters are about 4 GeV.

The energy resolution of BEMC for electromagnetic showers has been determined as $\sigma(E)/E = 10\ \%/\sqrt{E}$ with a constant term of 4 %, dominated by the uncertainties in the stack-to-stack intercalibration. From an analysis of the kinematic peak (see section 5) an uncertainty in the absolute energy scale of ± 2 % has been derived.

- The plug calorimeter (PLUG): It has been designed to close the gap of acceptance for the energy flow measurement between the beam pipe ($\theta \sim 0.6^0$) and the forward part of the LAC ($\theta \sim 3^0$). Due to space limitations a compact sampling calorimeter with a diameter of 0.7 m, consisting of nine copper absorber plates interleaved by eight layers of large area Si pad detectors was chosen. The total thickness is 4.25 λ. The energy resolution of the PLUG suffers from both the coarse sampling and the lateral and longitudinal leakage and is about 150 $\%/\sqrt{E}$.

- The instrumented iron: The iron yoke of the main solenoid magnet surrounds all major detector components of H1. The laminated iron slabs of the yoke leave gaps which are filled with a total of 16 layers of limited streamer tube chambers (LST) made from halogen-free plastic material (Luranyl), serving two purposes: In order to measure the hadronic energy leaking out of the LAC, eleven LST layers are equipped with readout pads (30×30 cm^2 and 50×40 cm^2 for the endcap and barrel regions, respectively). This set of pad layers is called the tail catcher (TC). Its performance has been studied in beam test measurements at CERN, where an energy resolution of $\sigma(E)/E \approx 100\%/\sqrt{E}$ was obtained for π beams. The other function of the LST system is to survey penetrating muons, where the spatial resolution is based on the 1 by 1 cm^2 tube cross section. The total size of this central muon system is 4000 m^2 with 103,000 wires, covering the polar angular range $5^0 < \theta < 170^0$.

- The forward muon spectrometer: The purpose of this component is to measure high energy muons in the range of polar angles $3^0 < \theta < 17^0$. The detector consists of six planes of double layer drift chambers mounted on either side of a toroidal magnet, accepting muons in the momentum range 5 to 200 GeV/c. The expected momentum resolution varies from 24 % at 5 GeV/c to 36 % at 200 GeV/c.

- The time of flight (TOF) system: The TOF system is located upstream of the interaction region, behind the backward electromagnetic calorimeter BEMC, at $z \approx -2$ m, and consists of two scintillator hodoscope planes, sandwiched between 1 X_0 of lead to absorb synchrotron radiation. The area of the scintillator planes roughly matches the BEMC surface. The time resolution of the system is about 3 ns and enables the separation of genuine ep events from beam-wall and beam-gas interactions upstream of the detector at the trigger level, which have a mean separation in time of about 13 ns. In addition to the TOF device two double scintillator veto walls, shielded against synchrotron radiation by 4 mm thick lead sheets, are installed upstream from the interaction point. The smaller inner veto wall, at a distance $z = -8.1$ m, covers the near beam area down to a radius of 11 cm with total area of 100×90 cm^2. The large outer veto wall, positioned at $z = -6.5$ m, with an area of about 5×4 m^2, overlaps the inner veto wall and nearly all of the LAC and the instrumented iron end caps. Hard penetrating off-axis particles from upstream are identified by coincidence of the two veto walls with a time resolution of ± 3 ns.

- The luminosity system: The luminosity monitor,[20] is designed to detect the $e - \gamma$ coincidence from the Bethe-Heitler process $e + p \rightarrow e + \gamma + p$, and consists of two components. The electron tagger is located at $z = -33$ m from the interaction region and detects electrons with energies E' in the range $0.2E < E' < 0.8E$, scattered through polar angles below 5 mrad with respect to the electron beam direction. The photon tagger is located at $z = -103$ m. Both detectors are TlCl/TlBr crystal calorimeters with an energy resolution of $\sigma(E)/E = 10\%/\sqrt{E}$ and a space resolution of $\sigma(x,y) = 0.2$ cm. The geometrical acceptance of the photon detector for bremsstrahlung photons is $\sim 98\%$. The uncertainty of the luminosity measurement amounts to 7%, limited by the present experimental knowledge of the electron beam tilts $\Delta\theta_{x,y}$.

A vital aspect of the ep experiments at HERA is triggering. Most of the many subdetectors presented above produce trigger information so that a trigger decision can be made, for every bunch crossing of 96 ns, according to basic physics quantities. However, background events (beam-gas or beam-wall) originating from strong interactions usually outnumber the interesting physics events by several

Table 1: *Summary of H1 Multilevel Trigger System*

Level	Information	Use	Timing	Max. Rate on Output
L1	8 bit energy $\sum$'s tracking info etc.	discriminators hardwired logic	deadtime free 2.2 μs pipeline	5000 Hz
L2	8 bit energy $\sum$'s tracking info etc.	pattern recogn. with NN/TT	20 μs	100 Hz
L3	full trigger data	μ proc. based pattern recogn.	2 ms (max)	50 Hz
L4	full data	RISC farm	30 ms	10 Hz

orders of magnitude. To allow decisions of increasing complexity and therefore to limit the data taking rate to an acceptable level of $O(10$ Hz), H1 is equipped with a multi-level trigger system, consisting of two hardware and two software levels: The deadtime-free, pipelined level 1 trigger is followed by two levels of synchronous trigger systems (level 2 and level 3) which operate during the primary deadtime of the front end readout, and one asynchronous event filter system (level 4), consisting of a fast processor farm with access to the full event information allowing complete online event reconstruction. The levels 2 and 3 have access to the complete level 1 information of all subdetectors and can therefore exploit correlations among these quantities. For the level 2 various hardware solutions are under construction including a neural network trigger (NN)[21] and a complex topological trigger (TT).[22] A summary of the four stages of triggering is shown in Tab. 1.

4 Photoproduction

Electron-proton collisions at low Q^2 provide a unique source for reactions of quasi-real photons on protons. Photoproduction at HERA has a large variety of applications, ranging from the copious production of heavy flavours to detailed studies of QCD in the perturbative and non-perturbative regime. In addition, the partonic structure of the photon can be investigated in hard scattering processes. Due to the large cross section, photoproduction constitutes a major background for many other reactions at HERA so that a detailed understanding is mandatory also from the purely experimental point of view.

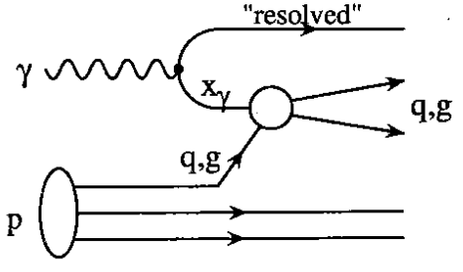

Figure 4: *Leading order QCD hard γp interaction of the constituents of a "resolved" photon with the partons from the proton, leading to at least two high p_T jets plus two low p_T remnants from the photon and the proton.*

Phenomenologically, γp scattering can be viewed as a superposition of several production mechanisms, related to the structure of the photon[24]: The bulk of the cross section is "soft", leading to low p_T particle production, described by the vector dominance model (VDM).[25] According to VDM the photon couples to hadronic vector particles (ρ, ω, ϕ ...) which in turn interact strongly with the hadronic collision partner. In photoproduction, however, also high p_T particles can be produced. They are thought to result from a hard scattering process of the hadronic constituents of the photon ("resolved photon"), characterized by a structure function $F^\gamma(x_\gamma)$, with the proton constituents. The corresponding lowest order diagram is shown in Fig. 4. In contrast to real hadrons, photons can also couple directly to quarks (see diagrams in Fig. 5 for QCD Compton scattering and boson-gluon fusion) which leads to at least two jets in the final state. The proper relative contributions ("matching") between the latter "hard" scattering processes described by perturbative QCD and the former "soft" VDM part is an

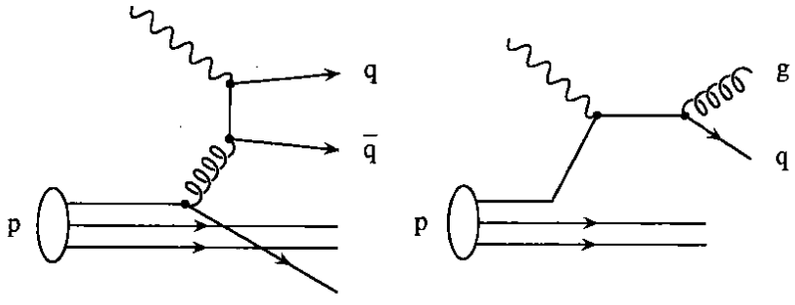

Figure 5: *Direct interactions of the incident photon with the constituents of the proton, giving rise to at least two high p_T jets ($O(\alpha_s)$: QCD Compton and boson gluon fusion) plus a low p_T remnant of the proton*

important issue in the description of high energy photoproduction.[24]

4.1 Total Cross Section

Before HERA, the available center-of-mass energy available for photon-proton interactions was limited to 18 GeV.[26] Some years ago, the observation of an excess muon yield in ultra-high energy cosmic air showers[27] has led to speculations about an anomalous hadronic interaction of the photon at very high energies (minijet models[28–30]). In some of these models the ansatz

$$\sigma(s) = \sigma^{\rm soft} + \sigma^{\rm jet}(s)$$

with an energy-independent soft part is used. The minijet cross section is cut off by $p_T^{\rm min}$, the minimum transverse jet momentum down to which the perturbative QCD calulation is assumed to be valid. Depending on the photon structure function and the minimum cut-off for p_T, cross sections as large as about 750 μb are predicted at HERA energies. In such models the cross section is driven by the rapid increase of the gluon density both in the resolved photon and the proton at small x, possibly even showing saturation effects already at HERA energies. In contrast to the minijets, conventional Regge-motivated extrapolations from the low energy data predict a cross section around 170 μb.[31]

The γp cross section measurement at HERA is based on the single photon exchange approximation of the low Q^2 ep scattering process. Using the Weizsäcker-

Williams approximation (WWA),[32] the total photoproduction cross section $\sigma_{\rm tot}^{\gamma p}$ used by H1 is given by

$$\frac{d\sigma_{ep}}{dy} = \sigma_{\rm tot}^{\gamma p}(W_{\gamma p})\frac{\alpha}{2\pi}\frac{1+(1-y)^2}{y} ln\frac{Q^2_{\rm max}(y)}{Q^2_{\rm min}(y)},$$

where $Q^2 = -q^2$ is the momentum transfer squared from the initial electron of energy E to the scattered electron of energy E' (Q^2 is also called the "virtuality" of the photon) and $y = 1 - E'/E$ is the photon energy in units of the incident electron energy. Denoting the proton energy by E_p, the γp center-of-mass energy is given by $W_{\gamma p} = \sqrt{4yEE_p}$ and $Q^2_{\rm min} = (m_e y)^2/(1-y)$, with m_e being the electron mass. The value $Q^2_{\rm max}$ is determined by the experimental conditions. In order to determine the total cross section two methods are possible. One may either use only tagged events, where the energy of the scattered electron in measured in the H1 small angle electron tagger (polar angle $\theta < 5$ mrad with respect to the electron beam direction), or use untagged events where the electron is not observed (5 mrad$< \theta < 70$ mrad, i.e. the scattered electron escapes in the beam pipe or does not enter into the detector acceptance region).

For tagged events, the kinematic range is given by the acceptance and the trigger threshold for the electron tagger (for details see[20]):

$$0.2 < y < 0.8 \qquad (13)$$

$$3 \times 10^{-8} < Q^2 < 10^{-2}{\rm GeV}^2. \qquad (14)$$

Using the tagged event sample offers the possibility to determine the photon energy y with good precision and therefore to know the actual value of the γp center-of-mass energy $W_{\gamma p}$ within the range $90 < W_{\gamma p} < 290$ GeV, given by eqn. (13). In contrast to this, the y measurement based on the observed hadrons, as in the case of untagged events, is poor.

The two methods access different, but overlapping, kinematical regimes and are recorded by different triggers. Although the untagged sample has less precision for $W_{\gamma p}$ and larger corrections to the WWA (about 12 % vs. < 0.3 % in the tagged case because of the larger $Q^2_{\rm max}$), it serves as an important cross check for the tagged measurement. Details of the experimental procedures can be found elsewhere.[20,34] A first measurement of the total photoproduction cross section by H1 was based on only 1.5 nb^{-1} from the early 1992 data.[20] Figure 6 shows the result using 21.9 nb^{-1} taken in 1992, which corresponds to $< W_{\gamma p} >= 197$ GeV:

$$\sigma_{\rm tot}^{\gamma p} = 156 \pm 2({\rm stat}) \pm 18({\rm syst})\mu{\rm b}$$

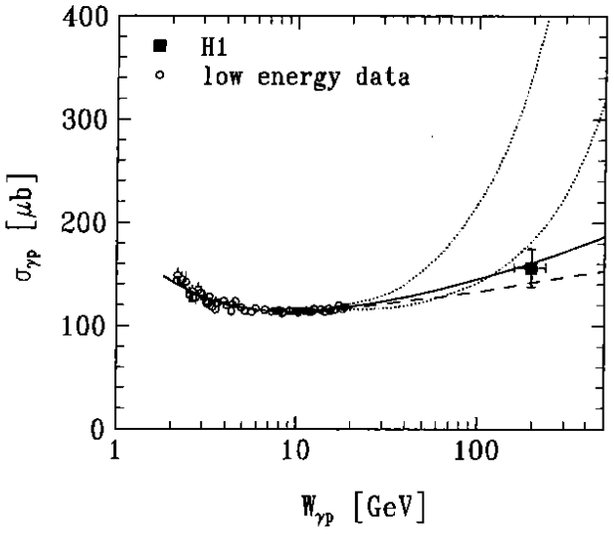

Figure 6: *Measurements of total photoproduction cross section at an average center-of-mass energy of 197 GeV. Also shown are the low energy data together with a Regge-motivated fit*[31] *(solid line), the prediction of the ALLM parametrization*[35] *(dashed line) and two variants of a model (see text) with* $p_T^{\min} = 1.4$ *GeV/*c^2 *(upper dotted line) and* $p_T^{\min} = 2.0$ *GeV/*c^2 *(lower dotted line), using the DG*[36] *parametrisation of the photon structure function.*

The dominant contributions to the systematic error come from the uncertainties in the luminosity (6 %) and the detector acceptance (10 %). The latter is driven by uncertainties in the modelling of the underlying processes which make up the total γ proton cross section: "Soft" and "hard" processes have quite different acceptances and their relative contributions to the total cross section must be input to the acceptance calculations a priori. Further reduction of the systematic error will result from a better understanding of the mix between diffractive and non-diffractive parts in the cross section. The H1 data, as well as a similar measurement from the ZEUS Collaboration,[37] show no unexpected energy dependence, the Regge-motivated extrapolations from low energies, using a universal Pomeron exchange picture, are in good agreement with the HERA data. The extreme minijet models ($p_T^{\min} < 2$ GeV/c^2) are clearly excluded.

4.2 Exclusive ρ Production

Measurements of $\gamma p \to \rho p$ at high energies allow testing the universality of the Pomeron properties, found to be very successful in the description of the total photoproduction cross section. Also in minijet models for $\sigma_{\rm tot}^{\gamma p}$ the reaction $\gamma p \to \rho p$ is uniquely fixed.[30]

Measurements of elastic photoproduction of vector mesons with the H1 detector rest mainly on the central tracking system, where pions and kaons can be discriminated on the basis of dE/dx in the jet chambers. Clear ρ and ϕ signals can be established. Due to the chamber acceptance, elastic ρ production is limited to $20 < W_{\gamma p} < 80$ GeV. Inelastic and target fragmentation (diffractive) processes are suppressed by requiring no energy deposition outside the areas tagged by the vector meson decay products. Monte-Carlo calculations show that the experimental cuts applied leave a contamination of less than 10 % from diffractive processes in the elastic ρ sample for four-momentum transfers squared $|t| < 0.4$ GeV^2. The t distributions for the reaction $\gamma p \to \rho p$, divided into two bins in $W_{\gamma p}$ with approximately equal statistics, were fitted to the form $d\sigma/dt = ae^{bt}$. The resulting slopes are $b = 9.4 \pm 1.1$ GeV^{-2} and $b = 11.1 \pm 1.3$ GeV^{-2} for $W_{\gamma p} = 20 - 40$ GeV and $W_{\gamma p} = 40 - 75$ GeV, respectively.

4.3 Hard Scattering

Photoproduction of high $p_{\rm T}$ particles or jets in principle receives contributions from processes where the photon couples directly to the partons within the proton, or where the constituents of the photon ("resolved photon") interact with those of the proton. In leading order $O(\alpha\alpha_s)$ two jets are produced, balancing each other in $p_{\rm T}$, while the scattered electron is hardly deflected and stays in the beam pipe. Already with the first nb^{-1} of HERA data at $W_{\gamma p} \approx 200$ GeV the resolved photon component, predicted by QCD, was firmly established in ep scattering.[39,40] Qualitatively, the resolved photon component is expected to dominate[41] in the $p_{\rm T}$ range below a few GeV/c.

In the analysis of charged particle spectra, the tagged events from the 1992 run were used. Figure 8 shows the data from H1[42] on the differential cross section $d^2\sigma/d\eta dp_{\rm T}^2$ for charged particles as a function of $p_{\rm T}$, measured in the kinematic region of pseudo-rapidity ($\eta = -\ln\tan(\theta/2)$) $|\eta| < 1.5$, $Q^2 < 10^{-2}$ GeV^2, and $0.3 < y < 0.7$, at an average γp center-of-mass energy of about 200 GeV. Clear

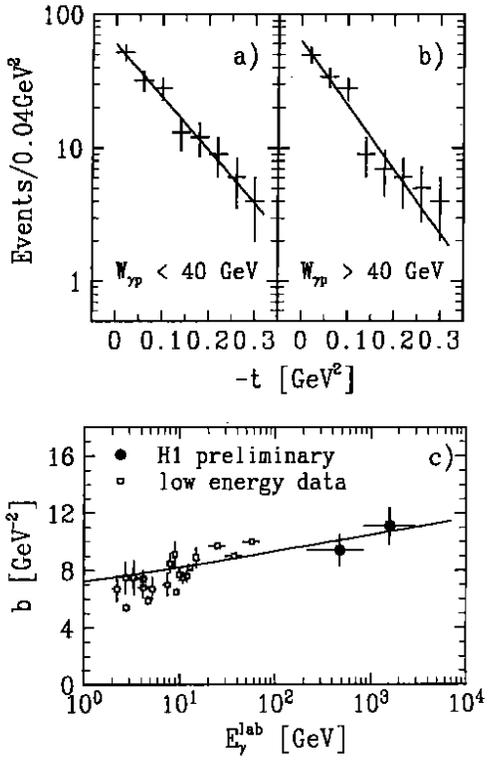

Figure 7: *a) and b) Slope parameter for elastic ρ production in two different bins of the γp center-of-mass energy. c) measurements of the slope parameter b (see text) for elastic ρ photoproduction from H1, compared to the low energy data. The line shown represents a phenomenological parametrization of the energy dependence of the slope b.*[24]

evidence for tails in the high p_T domain is seen. A Monte Carlo calculation using PYTHIA[43] with a p_T^{min} cutoff of 2.3 GeV/c for the hard γp scattering process which incorporates the resolved photon QCD component (for the low p_T part the Monte Carlo program RAYPHOTON[44] was used) is in good agreement with the data. In these simulations the Drees-Grassie[36] parametrisation of the photon structure function and the M-T B1[45] proton structure functions were used. Also shown in the figure is the shape of a next-to-leading (NLO) order QCD calculation[46] (solid line), normalized to the data, which assumes the resolved photon component to dominate. Compared to data from pp interactions at similar center-of-mass energies,[47] the γp data show a significantly more pronounced high p_T tail. This is a reflection of the direct interaction of the photon with the charged partons of the proton, a component missing in hadron-hadron collisions, where only the "resolved" constituents interact.

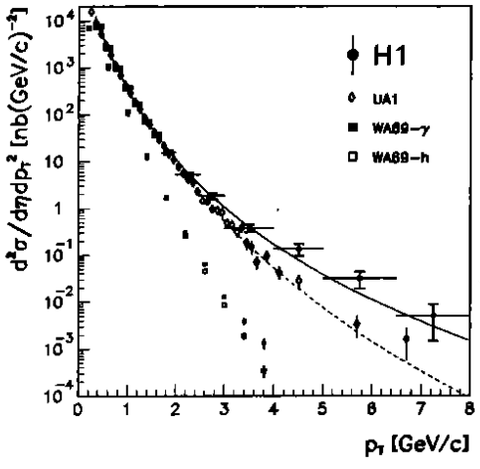

Figure 8: *Measured differential cross section in the range $-1.5 < \eta < 1.5$ (filled circles), compared with measurements of the UA1 Collaboration (open diamonds) at E_CM = 200 GeV for a comparable η range of 0 to 3.2, normalized to the H1 data at p_T = 300 MeV/c. The curves indicate power-law fits to the data (see text).*

4.4 Inclusive Jet Cross Sections

Evidence for a two jet structure in the photoproduction data is given in fig 9, where the tranverse energy E_T from the calorimeter is used as a measure for the hardness of the interaction. In the figure the distance in the azimuth $\Delta\phi$ of charged particles with respect to the leading particle in p_T is plotted, with the total observed E_T as a parameter. As the E_T threshold is raised, one observes an evolution of the $\Delta\phi$ distribution towards a clear back-to-back topology, peaking at $\Delta\phi = 0$ and 180 degrees.

Within the presently accessible kinematic range for photoproduction at HERA the resolved photon component dominates the jet cross section, as can be inferred from the single particle spectra discussed above. This component is described by the photon structure function which so far has been studied only in deep inelastic $e\gamma$ scattering at e^+e^- colliders. Jet production in untagged $\gamma\gamma$ collisions[48] has been

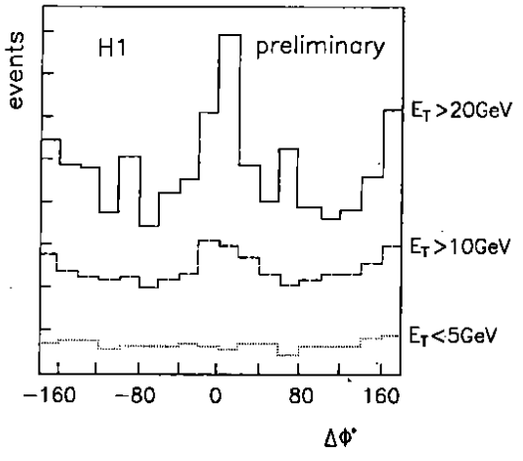

Figure 9: *Distribution of distance $\Delta\phi$ in azimuth of charged particles in an event from the leading p_T charged particle as a function of total E_T measured in the calorimeter. Back-to-back clustering, characteristic for two-jet production, is clearly observed when E_T is raised above ≈ 10 GeV.*

shown to be marginally sensitive to the gluon content of the photon. Moreover, the theoretical uncertainties in the QCD calculations of jet cross sections are limited by the relatively low E_T in these collisions. Therefore measurements of high E_T jet production at HERA will provide valuable information of the photon's gluon content and enable more stringent tests of QCD.

The jet finding algorithm applied to the tagged events ($0.25 < y < 0.7$, corresponding to $W_{\gamma p} = 150 - 250$ GeV) follows the "Snowmass accord"[49] and is based on the transverse energy in the calorimeter contained in the cone of radius $R = \sqrt{(\Delta\eta)^2 + (\Delta\phi)^2} = 1.0$, where $\Delta\eta$ and $\Delta\phi$ (in radians) are pseudo-rapidity and azimuth intervals. Only jet cones with $E_T > 7$ GeV and $-1 < \eta < 1.5$ were accepted for the final analysis. Figure 10 shows the corrected inclusive jet cross section as function of E_T and of pseudorapidity η. The inner error bars represent the statistical errors only, the total errors result from adding the systematical bin-to-bin errors in quadrature to the statistical ones. An additional overall uncertainty in the cross section normalisation of 40 %, dominated by the calorimeter energy scale uncertainty for hadronic jets (see section 3), is not included. The cross sections fall steeply with increasing transverse energy approximately as $E_T^{-5.5}$, and rise strongly with η, i.e. towards the forward (proton beam) direction.

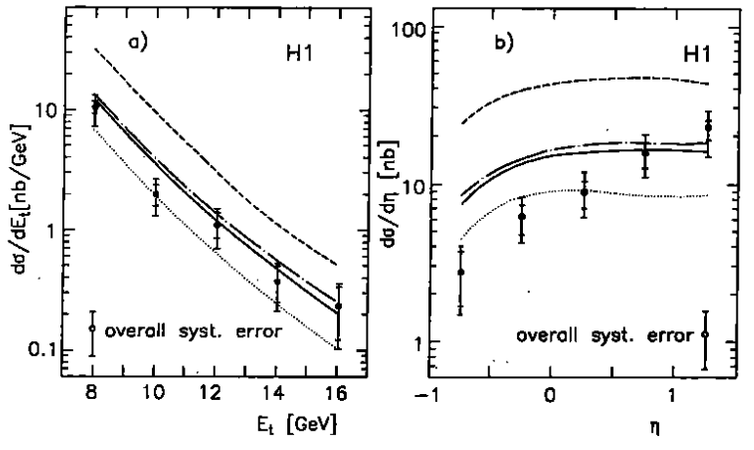

Figure 10: *a) Inclusive Jet E_T spectrum, integrated over the pseuorapidity interval $-1 < \eta < 1.5$. b) Inclusive η spectrum for jets with $E_T > 7$ GeV. The inner error bars represent the statistical errors, the outer error bars show statistical and systematic errors added in quadrature. The overall systematic uncertainty of ±40% is indicated. The curves show leading-order QCD calculations in the framework of the PYTHIA event generator using the photon structure functions LAC-3 (dashed line), LAC-2 (dashed-dotted line), GRV-LO (full line), and GRV-LO, but excluding the gluons originating from the photon (dotted line).*

To show the sensitivity of our data to the photon structure function, three leading order QCD parametrisations[53,52] of the deep inelastic $e\gamma$ scattering from e^+e^- experiments, differing mainly in their gluonic content, are also shown in fig. 10. The large uncertainty in the gluon content results from the fact that the e^+e^- data, in contrast to high p_T photoproduction, are sensitive to the gluons only indirectly through the Q^2 evolution of the photon structure function. Note that the predictions are independent of the chosen cutoff in PYTHIA of $p_T^{min} = 2.3$ GeV (the jets all have $Et > 7$ GeV) and are hardly affected by the uncertainites of the proton structure function, for which a leading order parametrisation[51] was chosen (85 % of the jet sample has a Bjorken $x > 0.01$, well covered by recent experiments[50,3]). The shape of $d\sigma/dE_T$ is well described by all the models in the η range covered. However, the cross section calculated using LAC-3,[53] which

exhibits a large gluon content in the photon at high x_γ, exceeds our data by roughly a factor of three. On the other hand, our data do demand some gluon content, as demonstrated with a calculation based on the parametrisation of Glück et al.,[52] from which the gluon content inside the photon has been excluded.

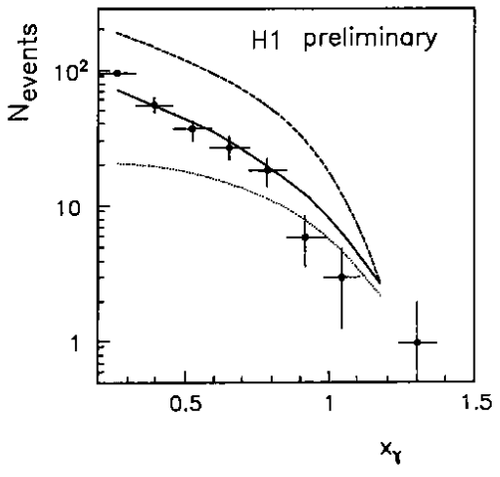

Figure 11: *Distribution of the photon Bjorken x for hard photoproduction ($E_T > 5$ GeV and $|\eta| < 2.5$). The curves correspond to the expectations based on various choices of the parton distribution functions $F_2^\gamma(x, Q^2)$ for the photon: LAC-3[53] (dased line), GRV-LO[52] (solid line), and GRV-LO with gluons removed (dotted line).*

4.5 Partons inside the Photon

A first attempt to extract the partonic structure of the photon (x_γ distribution) from the photoproduction data is shown in fig. 11. The parton x_γ is measured in final states with two high p_T jets (see fig. 10) of transverse energy E_{T_i} and polar scattering angles θ_i with respect to the proton beam direction, using the approximate relation

$$x_\gamma \approx \frac{E_{T_1} \tan\frac{\theta_1}{2} + E_{T_2} \tan\frac{\theta_2}{2}}{2E_\gamma}. \qquad (15)$$

The overspill of the distribution for $x_\gamma > 1$ is caused by the limited jet resolution and the accuracy of the above formula. The x_γ distribution in the figure is shown together with the expectations of the parametrisations extracted from the QCD analyses of the deep inelastic $e\gamma$ scattering data.[53,52] Again, our data do not support the choice of a large gluon content inside the photon at large x_γ.

Vice versa, suppressing entirely the gluon content is also in conflict with the measurements. These findings are in agreement with a recent QCD analysis of e^+e^- data from KEK[48] and with our measurements of the differential jet cross sections shown in fig. 10.

5 Deep Inelastic Scattering

Precise measurements of deep inelastic scattering (DIS) of charged[54,50] and neutral[55] leptons on nuclear matter have been essential for our understanding of the partonic substructure of the nucleon. These measurements have provided stringent tests of QCD. While QCD in its present form cannot supply information on the parton distribution functions inside the nucleons, it does predict the Q^2 evolution of the structure functions. Recently, theoretical interest has focussed on the behaviour of the parton distribution functions at low values of Bjorken x, where nonperturbative effects are expected to become noticible.[8] It is likely that the linear DGLAP equations[56] for the Q^2 evolution of the parton density functions will have to be replaced by nonlinear equations[8,57] as the parton density rises strongly in the transition region between the perturbative and nonperturbative regimes. Fixed target experiments have been limited to values of $x > 8 \times 10^{-3}$, whereas the high center-of-mass energy of about 300 GeV at HERA allows extending the x range down by an order of magnitude, where one can hope to test the new theoretical ideas. One important experimental input to this study is the measurement of the structure function F_2 in the low x ($< 10^{-2}$) region at HERA energies, for which extrapolations from the low energies are available, using parton density parametrizations evolved by the (linear) DGLAP equations. In the absence of data for $x < 10^{-2}$ the parametrizations have to make assumptions on the low x behaviour. Basically two limiting prescriptions exist: Either the so-called "Regge-type" behaviour with a flat F_2 as x goes to zero, or the "Lipatov" behaviour,[57] exhibiting a strong rise of F_2 at small x mainly driven by the gluon density, which is assumed as $g(x) \sim x^{-\lambda}$ with $\lambda \sim 0.5$. These behaviours have been incorporated into a number of parametrizations such as MRSD[58] with Regge-type (MRSD0) or Lipatov-type (MRSD-) gluon densitites, CTEQ1MS,[60] GRV,[51] DOLA[59] and others. Clearly, a strong Lipatov rise of the gluon density will make the observation of novel effects at HERA energies more likely.

A high Q^2 DIS event, typical for the data sample taken in the runs of 1992

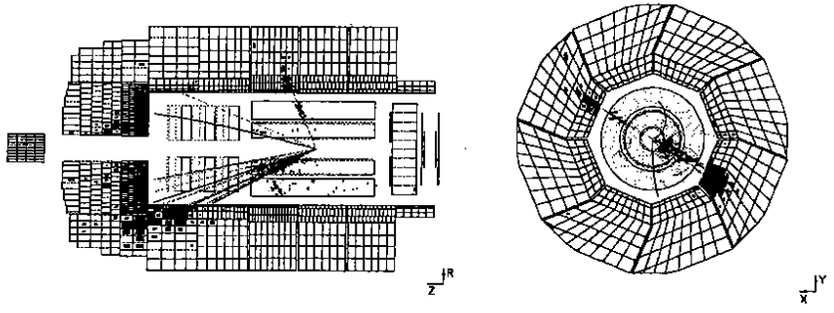

Figure 12: *Deep inelastic scattering event in the H1 detector. The electron is scattered into the LAr calorimeter. The kinematical variables are* $Q^2 = 5170$ *GeV*^{2}, $y_e = 0.23$, $x = 0.26$.

and 1993 is shown in fig 12, with the electron scattered into the LAr calorimeter and a clear jet final state observed in the forward part of the LAr calorimeter and the central trackers. The event trigger for these neutral current (NC) events rests mainly on substantial local energy deposition by the electromagnetic shower of the scattered electron in the calorimeters (typically $E_e > 4(5)$ GeV in BEMC (LAr)), thus avoiding any trigger bias in the hadronic final state. Trigger efficiencies of > 99 % are achieved. To fight background events from upstream collisions the veto from the TOF counters was essential: It reduced the trigger rate from BEMC, caused by off-axis-particles (beam halo), by about two orders of magnitude. Furthermore a vertex cut was applied to ensure events from the interaction region.

Due to the photon propagator in the scattering amplitude (see eqn. (16) below), the majority of DIS events is expected at low Q^2, low x, and high y, were the electron is hardly deflected. The events are selected by requiring an electromagnetic cluster in BEMC ("low Q^{2n}" sample, $Q^2 < 100$ GeV^2) or in the LAr calorimeter ("high Q^{2n}" sample), with at least 8 GeV deposited energy. The electron is quite loosely defined as a compact cluster, associated with hits in the tracking chafnbers. Experimental details of the selection procedures can be found elsewhere.[61–63]

The dominant background for DIS events is photoproduction, outnumbering by several orders of magnitude the deep inelastic collision rate. From γp collisions (see section 4) no scattered electron is expected in BEMC. However, hadrons produced in the reaction may lead to a signal in BEMC and fake a deep inelastically scattered electron. The size of this background is determined by detailed Monte Carlo simulations based on the γp generators PYTHIA and RAYVDM[44] describing hard and soft processes at $Q^2 \approx 0$, respectively, the relative contribution and overall normalization of which has been checked with our genuine photoproduction data.[20] An efficient cut against photoproduction events is the missing energy $E_{\mathrm{miss}} = E(y_e - y_h)$, which is expected to be around zero for non-radiating DIS events and large for the background: Photoproduction events will exhibit a mismatch between the kinematic variables determined from the electron and from the hadrons with $y_e \gg y_h$. For the selection a cut $E_{\mathrm{miss}} < 11.7$ GeV was chosen. Similar arguments hold for radiative DIS events which can also be suppressed by the E_{miss} criterion.

The kinematics of the inclusive deep inelastic scattering process $ep \to eX$ at fixed center-of-mass energy $\sqrt{s}$ is determined by two variables, conventionally chosen from the three independent quantities x, y and Q^2, which were defined by the equations (1-3). Since in the H1 experiment both the scattered electron and the hadronic final state produced by the struck parton and the proton remnant are observed, the collision kinematics can be reconstructed from the electron alone, (see eqns. (7,8)), the hadrons alone (see eqns. (10,11)), or from a mixture of both. Such a mixture is beneficial for the optimal measurement of the Bjorken variable x which depends on Q^2 and y (see eqn. (9)), as discussed above. For a precise measurement of the event kinematics the accuracy of the Q^2 determination is crucial. The resolution in Q^2, determined according to eqn. (7), is dominated by the energy resolution of the scattered electron and is therefore superior to the one based on hadronic energy measurement, or, to some extent, also to pure angle measurements ("double angle method", see e.g.[76]). A good understanding of the electron resolution in the BEMC is therefore crucial for all low Q^2 DIS analyses (the angular resolution, determined from the BPC, depends only weakly on θ). As could be seen from fig. 2, for a wide range of low Q^2 ($y < 0.5$) the energy of the scattered electron is close to the incident electron beam energy. This leads to a peak in the energy distribution of the scattered electron, the "kinematic peak", which is quite useful for calibration purposes (see also section 3) of the BEMC calorimeter. Since knowledge of the absolute energy scale is extremely important for the precision reconstruction of y and Q^2, much care has gone into the analysis of calibrating this detector. Figure 13 shows the kinematic peak in the electron

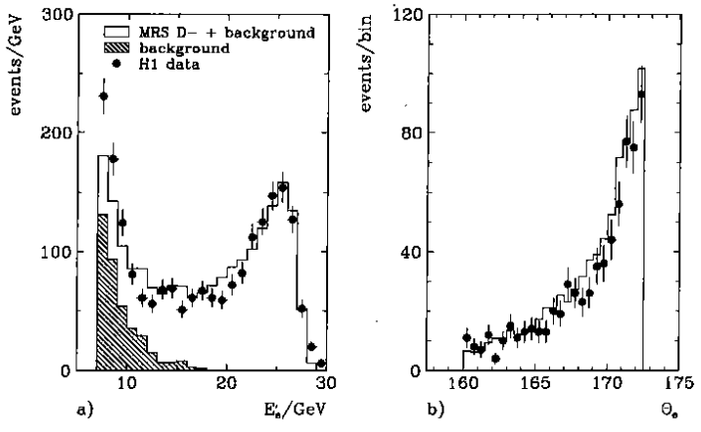

Figure 13: *Electron energy spectrum of the DIS events compared with a Monte Carlo simulation*[68,64] *of the H1 detector using the parametrization MRSD-.*[58] *The simulated spectrum is normalized to the measured integrated luminosity of 23* nb^{-1} *. Also shown is the background contribution from photoproduction events with a fake electron in BEMC.*

energy spectrum for the data, compared with a Monte Carlo simulation. The peak position is only weakly dependent on the underlying, a priori unknown, cross section of the data and can thus conveniently be used to calibrate the energy scale of the detector. Using this calibration method the energy scale of the BEMC for electrons is currently known to better than ± 2 %. The method was cross-checked by determining the electron energy from the angle of the electron and the current jet (see e.g.[65]).

5.1 Determination of $F_2^p(x, Q^2)$

For momentum transfers small compared to the mass of the Z^0 the cross section for deep inelastic electron-proton scattering in lowest order (Born cross section) can be expressed in terms of a single structure function F_2 and the ratio of cross sections for longitudinally and transversely polarized photons on protons, $R = \sigma_L/\sigma_T$:

$$\frac{d^2\sigma}{dxdQ^2} = \frac{2\pi\alpha^2}{Q^4 x}(2\,(1-y) + \frac{y^2}{1+R})F_2^p(x,Q^2). \qquad (16)$$

Since the ratio R, which in principle also depends on x and Q^2, has not yet been measured at HERA, the QCD prescription[66] for R with the parton density function MRSD- was chosen. The contribution from R, however, is only sizeable at large y, reducing the cross section in the present region of measurement by at most 8 % with respect to setting $R = 0$.

Two different methods have been used to determine the differential cross sections from which one extracts the structure function using eqn. (16): In method I the event kinematics is calculated from the scattered electron variables E_e and θ_e according to eqs. (7,8). Cross sections, acceptances and efficiencies are determined in bins of $\sqrt{E_e}$ and θ_e, matching the resolution and geometrical acceptance of the detector. The cross sections determined in these detector-oriented bins are then transformed to the "physical" bins x_e and Q_e^2. In method II a mixture of the hadron measurement of y (see eqn. (10)) and the electron measurement of Q^2 (see eqn. (7)) is used. As discussed above, method II is used in the low y region and method I for large values of y. Radiative corrections to the differential cross sections are applied using numerical results from the program TERAD[67] (method II) and the Monte Carlo programs HERACLES[68] and LESKO[69] (method I). Applying the E_{miss} cut (see above) for the events subjected to method I results in a significant reduction of the radiative corrections: While the corrections using the electron variables could exceed 100 % in the high y region, the E_{miss} cut reduces these to less than 10 %, with little sensitivity to the assumed form of the parton distributions. For method II the radiative corrections amount to less than 8 %, and an E_{miss} cut (which was not applied, however) would reduce the corrections even further. Comparison of the results from both methods constitutes an important check of the overall systematics involved in the determination of the structure functions with the H1 detector (the ZEUS Collaboration has presented their results[70] on $F_2^p(x, Q^2)$ using the double-angle method).

For the $F_2^p(x, Q^2)$ measurement from the "low Q^{2}" sample, consisting of 1026 events, the binning in x and Q^2 was optimized for studying the x dependence at fixed values of Q^2. The results[62] in four bins of Q^2 are shown in fig. 14. The systematic errors include possible shifts in the BEMC and LAr calorimeter energy scales (2 % and 7 %, respectively), energy resolution effects, uncertainties in the selection efficiencies due to fragmetation model dependence, background contamination, acceptance calculation, and radiative corrections, amounting to a total between 22 % and 15 % over the observed x range. An additional overall

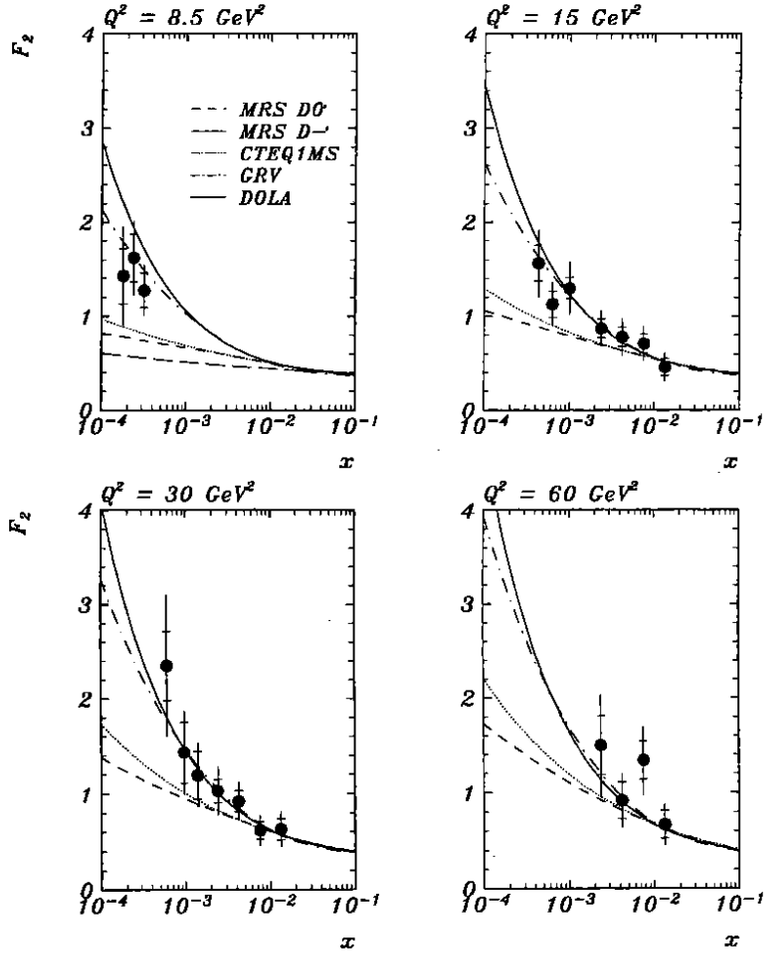

Figure 14: *Measurements of the structure function $F_2^p(x,Q^2)$ for different values of Q^2, compared to several parametrizations fitted to recent low energy data. The error bars are statistical (inner) and total (outer), obtained by adding the statistical and systematic errors in quadrature. All points have a common normalization uncertainty of 8 %.*

normalization error of 8 % from the electron trigger efficiencies, TOF veto, and vertex cut is not shown in the figure.

At $Q^2 = 8.5$ GeV^2 only the low x (large y) domain is accessible due to the limited angular acceptance of the BEMC and only method I can be used. At the highest Q^2 bin, $Q^2 = 60$ GeV^2, on the other hand, the high x (low y) domain is measured, based on method II with mixed variables which is more accurate here than the electron-only method. In the two intermediate Q^2 bins a comparison can be made between the two methods. The results from both methods which to a large extent are subject to quite different systematic effects, are found to be in good agreement. The high x data points also agree well with measurements from low energy experiments,[3,50] providing an important cross-check of our overall normalization with an accuracy of $\sim$ 20 %. It should be noted that even with the "low" statistics of 23 nb^{-1} from the 1992 data the errors are dominated by the systematics. A substantial reduction of these errors, however, will be possible in the future with more statistics, enabling a better control of the input parton distributions and fragmentation models for the selection efficiency and acceptance calculations, as well as a better understanding of the hadronic energy scale in the calorimeter.

From fig. 14 it is evident that F_2 rises strongly with decreasing x. Such a rise is not expected in Regge-type parton models. In a particular ansatz[57] for the gluon density, as discussed above, one expects a $1/\sqrt{x}$ behaviour for the structure function if the gluons are assumed to dominate at low x. On the other hand, linear evolution equations in perturbative QCD also predict a fast growth of the gluon density in the proton and therefore a growth[71] of $F_2^p(x,Q^2)$ which is faster than any power of $\ln(1/x)$ as $x \to 0$.

Also shown in fig. 14 are the expectations from various parton density parametrizations which all describe the existing low energy fixed target data for $x > 10^{-2}$. For $x \approx 10^{-4}$ they differ by more than a factor of 4. Our data are consistent with the GRV[51] and also the MRSD- (Lipatov-type)[58] parametrizations. Certainly it is not known a priori at which value of x the Lipatov behaviour should become visible or whether it will be masked by saturation effects. But exciting prospects are opened seeing $F_2^p(x,Q^2)$ rise at small x and QCD effects such as screening or saturation may in fact become detectable at HERA.

A fraction of the deep inelastic events exhibit the characteristics of missing energy deposit around the proton direction, which should generally be populated

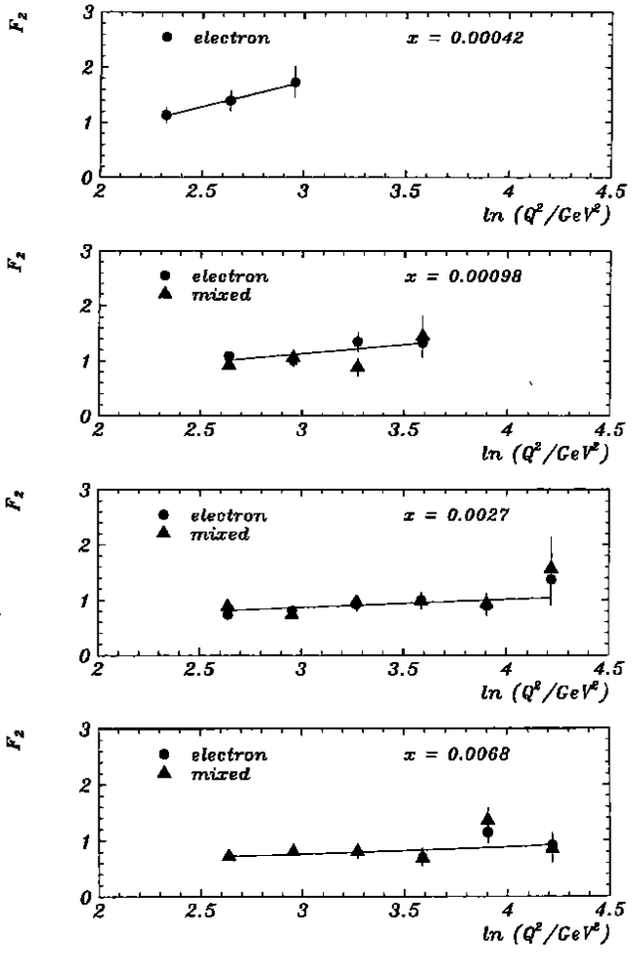

Figure 15: *The measured structure function $F_2^p(x,Q^2)$ for four different values of x, with statistical errors only. All points are subject to an overall normalization uncertainty of 8 %. The lines are straight-line fits to the electron data for $x < 0.001$ and to the mixed data at higher x.*

by the target fragments. These "rapidity gap" events (see below) are included in our F_2 measurements. A specific study shows that their fraction (about 6 % of the total sample) does not, within our statistics, significantly depend on either x or Q^2. They therefore play no special role in the rise of F_2 at small x.

5.2 Gluon Distribution

A more conventional prediction of QCD is the Q^2 evolution of $F_2^p(x,Q^2)$ at constant x. Our data[74] on the Q^2 dependence of $F_2^p(x,Q^2)$ are shown in fig. 15, exhibiting a slow rise with Q^2, a manifestation of the scaling violations as expected from perturbative QCD. The Q^2 dependence of $F_2^p(x,Q^2)$ at small values of x, presented in the previous section, can be related[72] in an approximative way to the gluon density $G(x,Q^2)$, following a procedure similar to the one extracting[73] $G(x,Q^2)$ from the longitudinal structure function $F_L(x,Q^2)$: Assuming, in the framework of the DGLAP evolution equations, the validity of perturbative QCD in the new kinematical regime of HERA the derivative of $F_2^p(x,Q^2)$ with respect to $\ln Q^2$, $\partial F_2/\partial \ln Q^2$, depends on the momentum weighted gluon distribution $G(x,Q^2)$:

$$\frac{\partial F_2^p(x,Q^2)}{\partial \ln Q^2} = \frac{5\alpha_s(Q^2)}{9\pi}\int_x^1 (w^2+(1-w)^2)G(x/w,Q^2)dw \qquad (17)$$

This relation is valid only for small x where the gluonic contributions are expected to dominate over the sea quarks and, of course, the valence quarks. From this equation a leading order estimate for the gluon distribution function can be obtained[72] from the measured derivatives of the structure function $F_2^p(x,Q^2)$:

$$G(2x,Q^2) = \frac{\partial F_2^p(x,Q^2)}{\partial \ln Q^2}\frac{27\pi}{10\alpha_s(Q^2)} \qquad (18)$$

Using parton distributions from QCD analyses at higher x we find that this relation holds to within 20 % for the present x range ($x < 10^{-2}$).

Since $F_2^p(x,Q^2)$ is observed to depend linearly on $\ln Q^2$ (see fig. 15) all data can be combined to yield $G(x,Q^2)$ at an average $Q^2 = 20$ GeV^2. For the calculation of $G(x,Q^2)$ from eqn. (18) we assume $\alpha_s = 0.24$, corresponding to four quark flavors, and $\Lambda_{QCD} = 200$ MeV. The resulting estimate[74] for the gluon distribution is shown in fig. 16 together with the expectations from different parametrizations of the gluon distribution, extracted from low energy DIS, Drell-Yan and photoproduction data. A similar measurement has been presented by the ZEUS

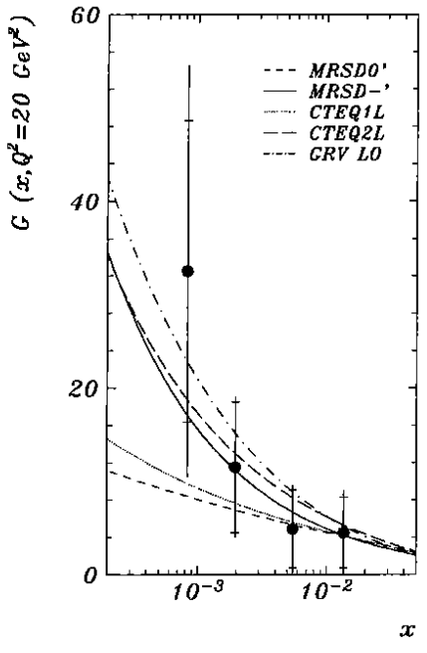

Figure 16: *The measured gluon distribution function $G(x,Q^2)$ at $Q^2 = 20$ GeV^2, compared to different parametrizations.*[58,51,60] *The errors shown are the statistical (inner) and total (outer) errors obtained by adding statistical and systematic errors in quadrature.*

Collaboration.[75] In working out the experimental data points, all errors have been correctly propagated through the data points of $F_2^p(x,Q^2)$ and their derivatives $\partial F_2/\partial \ln Q^2$. The neglect of the sea quark distributions is estimated to reduce $G(x,Q^2)$ by about 10 %, independently of the structure function parametrization. The experimental gluon distribution function $G(x,Q^2)$, although the errors are still quite substantial, is seen to rise steeply with decreasing x, consistent with the Lipatov behaviour $(1/\sqrt{x})$.

5.3 Hadronic Final State

In the simple quark parton model of deep inelastic ep scattering, a quark is scattered out of the proton by the virtual boson emitted from the scattering electron. In QCD this naive picture is modified by allowing for gluon radiation from the quark lines before (inital state radiation) and after (final state radiation) the boson quark vertex (see fig. 17). Furthermore, the boson may also interact with a gluon inside the proton through a quark line (boson gluon fusion). Such QCD effects should become visible in the hadronic final state. Expectations for the

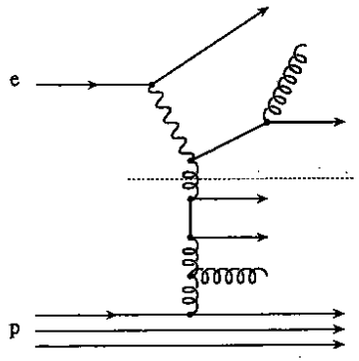

Figure 17: *Feynman diagram for DIS scattering with initial state (below the dashed line) and final state (above the line) parton shower.*

properties of the hadronic final state are available in the form of Monte-Carlo models, where the underlying parton level is based on QCD models, followed by hadronization models which transform the colored partons to colorless observable hadrons. Such models have been tuned to provide a satisfactory description of the low energy lepton nucleon data and the high statistics e^+e^- data from LEP. In the new kinematic regime of HERA the models differ widely in their predictions, most importantly in the (hardly tested) sector of inital state radiation.

In the Monte Carlo models the QCD emissions are generated based on essentially two prescriptions: either employing first order $(O(\alpha_s))$ QCD matrix elements, or generating a parton cascade to all orders in the leading logarithmic approximation. Also combinations of both approaches exist. For the comparison of the ep data below the following generators have been used:

- PSWQ[77]: Two parton cascades are generated, one from the time-like final state parton after the boson vertex, evolving analogously to parton radiation in $e^+e^- \to q\bar{q}$, and one from the space-like initial state parton before the boson vertex, which evolves "backwards" to the almost on-mass-shell parton in the incoming proton. No interference between the two cascades is considered. However, coherence effects in soft gluon emission, i.e. depletion of soft gluons due to destructive interference, for a given cascade is taken into account through angular ordering, which means decreasing the opening angles in subsequent branches with decreasing virtuality. The hardness of radiation for a branching process depends on the virtuality of the parent parton which are chosen between a lower cutoff and a scale given by the hadronic energy W or the momentum transfer Q of the process considered. Note that W and Q may be vastly different in DIS (in contrast to e^+e^-) and will therefore lead to differing predictions for the amount of gluon radiation. It has already been

shown by H1[61] that neither the scale W^2 nor Q^2 is favoured by the data: While the large scale $\langle W^2 \rangle \approx 10^4$ GeV^2 yields too much gluon radiation, the scale $\langle Q^2 \rangle \approx 15$ GeV^2 yields too little. A mixed scale WQ seems to fit the data best.

- MEPS[77]: Boson gluon fusion and gluon radiation are simulated using exact $O(\alpha_s)$ matrix elements. Higher order QCD effects, i.e. additional (soft) gluon emissions, are added using the parton shower approach. A cutoff is used to avoid kinematical regions where the matrix elements are divergent.
- CDM[78]: The color dipole model does not distinguish between inital and final state gluon radiation. Instead it describes gluon emission by a chain of independently radiating color dipoles, starting with a dipole formed between the color charges of the scattered pointlike parton and the extended proton remnant. This extended source leads to a suppression of gluon radiation with short wave lengths $\lambda = 2\pi/p_T$, where p_T is the transverse momentum of the emitted gluon with respect to the dipole axis. Note that this suppression occurs in the target region. Since all radiation is assumed to come from the struck quark and the proton remnant, boson gluon fusion cannot be generated this way and has to be added from QCD matrix elements.
- HERWIG[79]: This program is a general purpose event generator for hard lepton-lepton, lepton-hadron and hadron-hadron processes. It includes also soft hadron collisions able to simulate the soft remnants ("underlying event"). The QCD effects are implemented using parton showers with color coherence, this time taking into account the interference between inital and final parton cascades. The hadronization is modelled according to a cluster fragmentation algorithm, employing nonperturbative splitting of gluons into colorless clusters.

Hadronization for the above QCD Monte Carlo models, with the exception of HERWIG, is done by the LUND fragmentation scheme.[80] As a last ingredient, a parametrization of the proton structure function needs to be input to the simulations. This requires an iterative procedure, since the structure functions are the physical quantities one wants to measure at HERA. Nevertheless, a number of different parametrizations of low energy data, extrapolated to HERA energies, have been tried out. For the subsequent analysis of the hadronic final state in deep inelastic processes the MRSD$^-$ parametrisation[58] has been used which provides

an adequate description of the measured proton structure function (see above).

As examples of the ongoing H1 analyses, QCD effects in DIS events are studied in terms of the flow of transverse energy and of charged particles in the hadronic final state[61,81] for the 1992 data, corresponding to 22.5 nb^{-1} . As stated above, the main physics interest is in the small x region where new QCD effects might be expected. The distributions shown below are corrected for detector effects by applying appropriate bin-to-bin correction factors derived from detailed simulations of the detector response to DIS events. To ensure substantial energy in the hadronic final state a cut $W^2 > 3000$ GeV^2 was applied to the data. QED corrections have been studied using the HERACLES Monte Carlo[68] and have been found to contribute at most 5 %, generally much less. These effects have not been corrected for in the data but are included in the systematic errors.

5.3.1 Energy Flow

Figure 18 shows the corrected transverse energy flow $1/N dE_T/d\eta$, measured in the calorimeter, as a function of the pseudorapidity η, evaluated in the laboratory system. Note that the proton direction is to the right (positive values of η). In addition to the data the four QCD models as well as the naive QPM expectation is shown. QCD effects seem firmly established by the data. However, only the CDM seems to describe them in a satisfactory way while all the others fail.

The most natural frame to study the hadronic final state is the overall hadronic center-of-mass system (CMS). Denoting the transformed variables by a * as superscript, the z^* axis is defined in this frame as the direction of the exchanged virtual boson. In the QPM the current quark and target diquark system then correspond to the $+z^*$ and $-z^*$ directions, respectively. It is evident that the distribution of particle energies transverse to the z^* axis in the hadronic CMS is particularly sensitive to gluon radiation. As an example, the mean transverse energy $\langle E_T^* \rangle$, measured in the calorimeter, is shown in fig. 19 as function of W^2, which serves as an overall measure of the radiation activity. The mean transverse energy rises with increasing W^2, as expected from the increased phase space for gluon radiation. The slope of the rise is generally reproduced by the QCD models, but they differ in absolute normalization. A slight rise is also seen for the QPM, however, this can be attributed to the increased particle yield and consequently larger $\langle E_T^* \rangle$ at higher W.

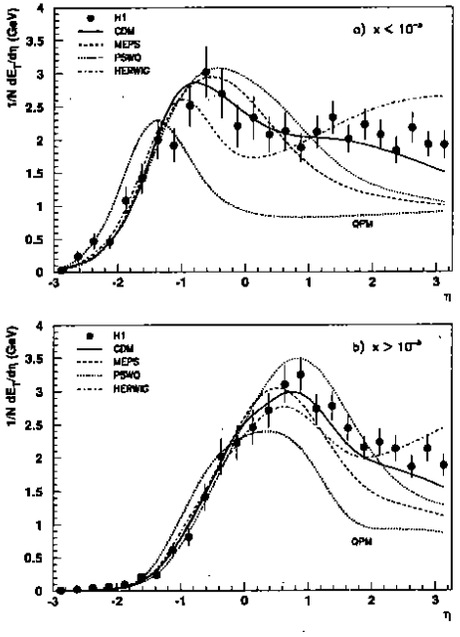

Figure 18: *Transverse energy flow E_T in the laboratory system as function of the pseudorapidity η, measured in the calorimeter, for events with $x < 10^{-3}$ and $x > 10^{-3}$. The proton direction is to the right (positive η's). The error bars contain the statistical and systematic errors added in quadrature, an overall uncertainty of 6 % in the energy scale is not included.*

5.3.2 Charged Particle Spectra

Single particle spectra for the longitudinal (p_z^*) and transverse (p_T^*) momentum components, measured in the hadronic CMS with respect to the virtual boson direction, provide further tests of QCD radiation effects. At HERA, contributions to the transverse momenta of particles from intrinsic p_T of the partons inside the proton and from fragmentation are expected to be small, leaving gluon radiation as the dominant source. A sensitive measure of this effect is the so-called seagull plot, which displays the average transverse momentum squared $\langle {p_T^*}^2 \rangle$ of the charged particles for a given longitudinal momentum p_z^* as a function of p_z^*. In order to become independent of W, the scaled longitudinal momentum $x_F = 2p_z^*/W$ is used here. The fully corrected H1 data[81] from a W interval between 50 and 200 GeV, corresponding to an average of $\langle W \rangle = 117$ GeV, are shown in fig. 20. The bin-to-bin corrections applied vary from 2 % at low x_F to 27 % at large x_F. Compared to the low energy data[82] at $\langle W \rangle = 14$ GeV the average p_T observed is

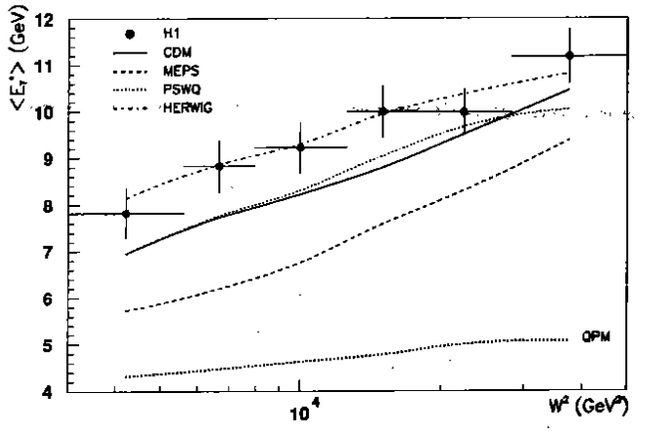

Figure 19: *Mean transverse energy in the hadronic CMS as function of W^2. The error bars contain the statistical and systematic errors added in quadrature, an overall uncertainty of 6 % in the energy scale is not included.*

much larger. The increase has to be attributed to QCD radiation, getting stronger as W rises. The QPM expectation, shown in the figure for comparison, yields a factor of 5 - 10 lower rate in $\langle {p_T^*}^2 \rangle$. Concerning the strength of the QCD radiation, the various models differ in their predictions, with MEPS and CDM providing an adequate description of the data.

5.4 Jet Production

Deep inelastic scattering from a proton constituent produces one or more (n) partons with large transverse momentum, giving rise to events with n high p_T jets plus a proton remnant jet, denoted as an $(n+1)$ jet configuration in the following. In lowest order QCD, i.e. in the QPM, a single quark is scattered out of the proton, leading to one current and one proton remnant (spectator) jet, a $(1+1)$ jet configuration. In an $O(\alpha_s)$ process, such as QCD Compton scattering or boson gluon fusion, two jets are produced in addition to the spectator jet, a $(2+1)$ jet configuration. On the parton level, exact QCD calculations to $O(\alpha_s^2)$

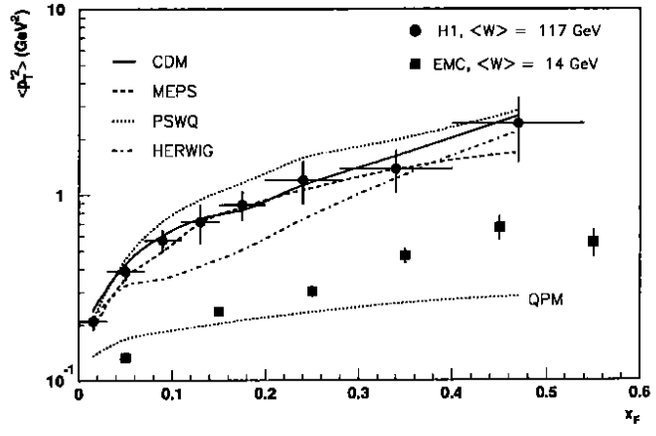

Figure 20: *Distribution of the average p_T^{*2} as function of x_F. p_T^* is evaluated in the hadronic center-of-mass system, with respect to the direction of the virtual boson. Various models are shown as well as the EMC data[82] at lower hadronic mass W.*

for DIS jet production have been performed[83] so that new precision tests of QCD can be envisaged. Most importantly, jet counting leads to the obvious possiblity of measuring the strong coupling constant α_s.

In order to make such QCD analyses meaningful the jets, which are thought to carry energy and directional information of the primary partons, have to be reconstructed from the hadronic final state. For this purpose the JADE cluster algorithm[84] has been used which was originally developed for e^+e^- interactions. This choice is justified also here, since good correspondence is observed in full simulations of DIS events between the parton level and the reconstructed jets. Furthermore, the algorithm is suited to recover jet final states of arbitrary multiplicity, useful for tests of future higher order QCD predictions. The algorithm uses as "particles" the individual calorimeter cells (energy and angles, forming a massless particle with four-momentum p_i) and accounts for the loss of particles in the beam pipe by introducing a pseudoparticle in the proton beam direction with the missing longitudinal momentum. The invariant masses of particle pairs are then calculated according to $m_{ij} = 2E_iE_j(1 - \cos\theta_{ij})$ and the two particles with the smallest mass are combined to a new object with four-momentum $p_k = p_i + p_j$.

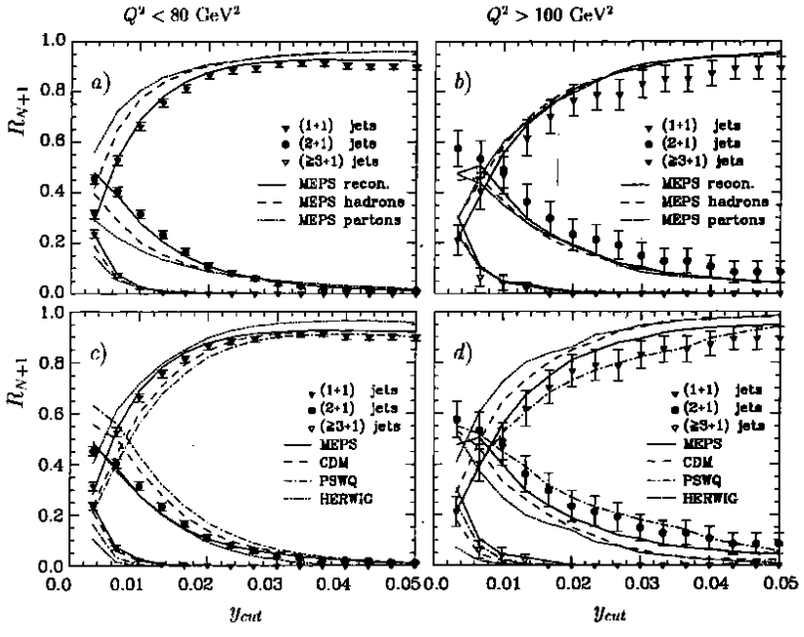

Figure 21: *Fractions of $N+1$ jets (R_{N+1}) versus the cut variable of the jet algorithm for $12 < Q^2 < 80$ GeV^2 (a),c)) and $Q^2 > 100$ GeV^2 (b),d)), compared in a),b) with simulations with MEPS at the detector level and at the parton level, and in c),d) to predictions from the QCD based models MEPS, CDM, PSWQ and HERWIG.*

This procedure is repeated until all pairs have masses $m_{ij} > y_{\rm cut}W'$, where W' is the hadronic mass including the pseudoparticle, and $y_{\rm cut}$ is a resolution parameter. The number of remaining clusters is a measure of the number of jets in the event.

The dependence of the jet rates on the resolution parameter, not corrected for detector effects, is shown[63] in fig. 21 for the low ($Q^2 < 80$ GeV^2) and high ($Q^2 > 100$ GeV^2) samples in comparison with several QCD models. Note that the data points are strongly correlated since the same events are used for each point; only the statistical errors are given. From the figures a) and b) one finds that

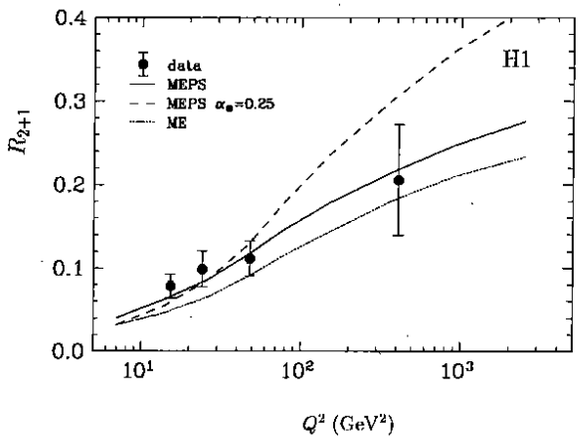

Figure 22: *(2+1) jet fractions (R_{2+1}) at y_{cut} = 0.02 versus Q^2, corrected for detector bias for $W^2 > 5000$ GeV^2 and $y < 0.5$, in comparison with the MEPS model with running α_s and a constant $\alpha_s = 0.25$, and also the matrix elements without parton showers (ME model). The data are plotted at the corrected $\langle Q^2 \rangle$ per bin. The error bars correspond to the statistical errors of data and Monte Carlo corrections.*

the dependences on hadronization and detector effects are small for $y_{cut} \geq 0.02$. For lower values of y_{cut} more structure at the hadron (or detector) level is found compared to the parton level: due to the small upper bound for the cluster mass in the algorithm, the jets may get fragmented , i.e. a $(1+1)$ event at the parton level may migrate to a $(2+1)$ event at the hadron level, thus precluding a "one to one" correspondence between parton and hadron level for a given event. While all QCD models generally describe the trend of the data in fig. 21, the $O(\alpha_s)$ matrix element (MEPS) model fits best. Note that none of the models was specifically tuned to the DIS data.

In a first attempt to gain insight into the strong coupling constant α_s in DIS, the Q^2 dependence of $R(2+1)$ was studied, where the resolution parameter $y_{cut} = 0.02$ was chosen. The experimental points are well described by the MEPS model and therefore detector correction factors could reliably be determined. Fig. 22 shows the corrected data for $R(2+1)$ together with several predictions based on the $O(\alpha_s)$ matrix element. In this representation, the rate $R(2+1)$ will rise with Q^2 because of the increased phase space available for gluon emission. On the

other hand on expects α_s to fall as Q^2 is increased ("running" α_s), entailling a falling $(2+1)$ jet rate. The two effects combine to produce a net rise if $R(2+1)$, but progressively falling short of the phasespace prediction (constant α_s) as Q^2 is increased. The observed $(2+1)$ jet rate in fig. 22 is mainly due to the γ-gluon fusion process, described by the first order matrix element (ME) with running α_s, corresponding to $\Lambda_{QCD} = 200$ MeV. Adding the parton shower to the matrix element (MEPS) to account for higher order effects slightly improves the agreement with the data. On the other hand, a constant α_s in the matrix element prediction is somewhat disfavored by the data. However, the present large statistical and systematic errors do not allow quantitative conclusions between a constant and a running α_s.

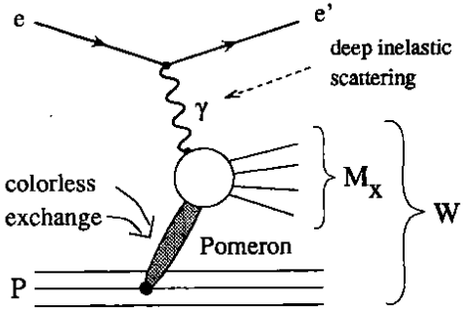

Figure 23: *Diagram for a deep inelastic event where the virtual photon scatters off a colorless object (Pomeron) inside the proton.*

5.5 Large Rapidity Gaps

A "standard" DIS event, as the one shown in fig. 12, exhibits energy flow associated with the direction of the proton, i.e. the forward direction. This flow presumably results from the fragmentation of the proton remnant, or in terms of the color string picture, from the fragmentation of the color string between the struck current quark and the proton remnant. ZEUS[85] have reported a class of DIS events with a lack of particles around the proton direction. Such events, in which no particle flow is observed in a interval of pseudorapidity ($\Delta\eta$) around the proton direction have also been found in the H1 experiment.[14,15] The observation of these "rapidity gap events", unexpected in the context of the color

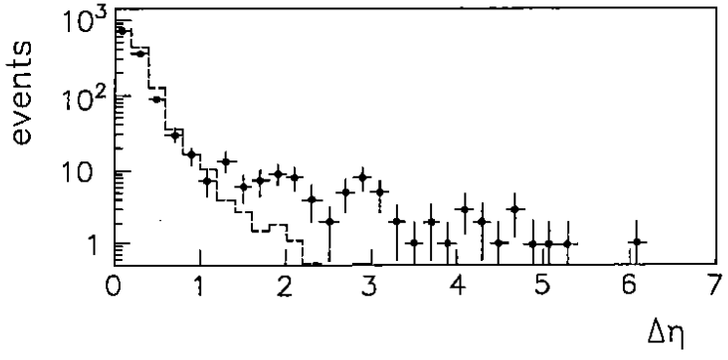

Figure 24: *Measured rapidity gap distribution for all deep inelastic scattering events, compared to the expectations from LEPTO (histogram). The spectra are uncorrected for experimental bias.*

string picture between the struck quark and the proton remnant, points towards a mechanism in which the virtual photon interacts with a colorless object emitted from the proton (see fig. 23). Such reactions can be viewed as diffractive processes involving Pomeron exchange, which have been studied for many years in hadron collisions.[86] For the case of ep collisions, diffractively produced hadronic final states have already been discussed in the literature.[87,7]

Figure 24 shows the distribution of the pseudorapidity gap, measured with respect to the forward egde of the LAr calorimeter, for all DIS events. The gap is defined as the difference in pseudorapidity between the acceptance edge and the most forward energy cluster larger than 400 MeV. Comparison with standard DIS Monte Carlo simulations (LEPTO) reveals a clear excess of events beyond $\Delta\eta \approx 2$. Events with such a rapidity gap amount to about 5 % of the deep inelastic sample. A number of checks have been carried out to ensure that these events are genuine DIS candidates. Most importantly, the study of possible contamination from electron-gas events and γp events has revealed that at most 1 % of the rapidity gap events may be explained by these background sources.

A prominent feature of all rapidity gap events is the small invariant mass of the hadronic system produced, which is shown in fig. 25. A non-negligible fraction of these events (about 5 %) have only 2 charged particles. The invariant mass of these predominantly oppositely charged particles, assumed to be pions, is typical for photoproduction of vector mesons and exhibits a clear signal from the ρ. This

observation supports the diffractive nature of the production process.

Preliminary studies of the uncorrected ratios of rapidity gap events to the total number of DIS with respect to Q^2 or x show no significant dependence on these variables. ZEUS[85] reported similar findings. However, one has to keep in mind that the selection procedure for rapidity gap events biasses the sample: Diffractive events with large Q^2 and/or high x will have little chance to be selected as rapidity gap events when the debris of the struck parton inside the Pomeron will be scattered into the forward direction and therefore populate the gap. Such effects have been observed with an event generator[88] designed to describe rapidity gap events. More data and a better understanding of the models employed will undoubtfully deepen our understanding of the underlying dynamics of hard diffraction in ep scattering.

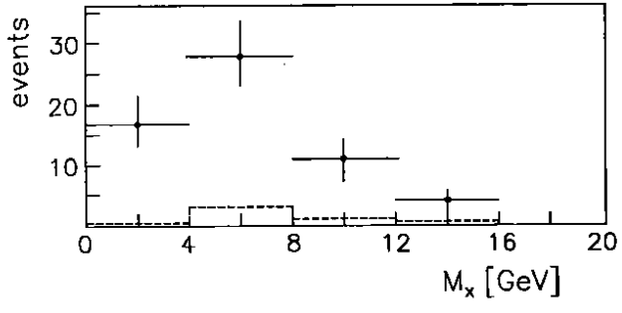

Figure 25: *Distribution of the invariant mass of the observed hadronic final state for the sample of rapidity gap events, compared with the standard DIS simulation (histogram). The spectra are uncorrected for experimental bias.*

5.6 Measurement of the Charged Current

One of the exciting areas of research opened up by HERA is the electroweak interaction between electrons and quarks. While the neutral current reactions in the kinematic regime presently accessible are still dominated by the electromagnetic interaction (photon exchange), purely weak processes, mediated by W exchange, can be studied in the charged current (CC) reactions $ep \to \nu X$. So far the charged weak current has been investigated only in fixed target neutrino experiments at

low CMS energies (for a review on these data see[23]), characterized by a cross section rising linearly with the neutrino beam energy. Charged current reactions at HERA are the inverse of these neutrino reactions, however, with a beam energy equivalent to about 50 TeV in the fixed target kinematics. At these high energies a significant deviation from the linear rise of the cross section is expected due to the finite mass of the W boson. The effect from the W propagator is huge, predicting a suppression of the cross section by a factor of three with respect to the linear extrapolation. From this it is clear that only a small number of CC events is sufficient to see the propagator effect.

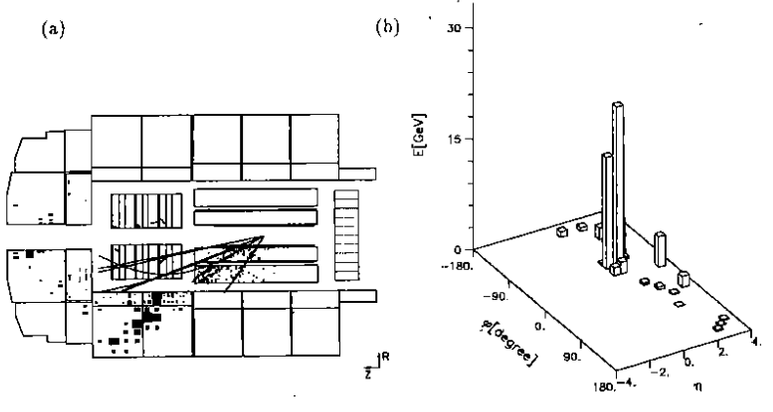

Figure 26: *A typical CC event in the H1 detector: (a) side view of the H1 tracking system with reconstructed charged particle tracks and the surrounding LAr calorimter with its energy depositions, (b) energy flow as measured in the calorimeter as a function of pseudorapidity η and azimuthal angle ϕ.*

Although the CC cross sections are very small owing to their weak nature, the event signatures are sufficiently distinctive to allow efficient reduction of an overwhelming background. However, after the first year of running which yielded 25 nb^{-1} just two candidate events for the charged current reaction were expected and found. A typical CC event, recorded by the H1 detector, is displayed in Fig. 26, showing the characteristic signature of a hadronic system unbalanced in transverse energy due to the unobserved neutrino. This signature allows sufficient

discrimination of CC events against other processes such as neutral current, γp and beam-gas reactions, which are approximately balanced. From the energy depositions of the final state hadrons in the calorimeter two observables can be computed, the scalar (S) and the vector (V) transverse momentum sums:

$$S = \sum_i |\vec{p}_{T_i}| \qquad V = |\sum_i \vec{p}_{T_i}|.$$

These quantities can be approximated by the total transverse energy and the total missing transverse energy measured from the individual calorimeter cells and the event vertex. Assuming a nominal position of the vertex, these quantities are also computed in the first level calorimeter trigger using the coarse granularity of 256 projective towers. The quantity V serves, together with a minimal vertex requirement from the MWPC's, as the main trigger for CC events. The trigger efficiency can be controlled purely from data using NC events where the electron is removed. These events have topologies of the hadronic final state similar to CC reactions and are an order of magnitude more frequent, owing to the photon propagator.

In an analysis based on an integrated luminosity of about 350 nb^{-1} , accumulated in 1993 *, CC candidates were selected with the requirement of $V > 25$ GeV, which seems a reasonable compromise between background rejection and statistics. In addition, radiative corrections are expected to be small for the Q^2 range beyond $Q^2 > 625$ GeV^2.

Radiating cosmic or halo muons deposit localized showers in the calorimeter, not balanced with respect to the vertex, and therefore constitute a serious source of background, most importantly when superimposed on a low Q^2 ep event. This background is largely rejected with the help of the moun chambers surrounding the LAr calorimeter. The automatic selection procedure yielded 19 candidates which were visually scanned for residual background. One halo and four cosmic muons were clearly identified, leaving 14 CC events. The fully corrected cross section for charged current reacions[89] with neutrino transverse momenta above 25 GeV, measured for the first time at HERA, is determined to be

$$\sigma(p_T > 25\text{GeV}) = 55 \pm 15 \pm 6 \quad \text{pb},$$

where the first error is statistical and the second error includes the various systematic uncertainties, dominated by the efficiency uncertainty, added in quadrature.

*This material has not been presented in the 1993 SLAC Summer Institute's Topical Conference.

This value can be compared to the theoretical expectation[90] of 40.9 pb for $p_T > 25$ GeV, in good agreement with the measurement. In the prediction electroweak and QCD corrections have been taken into account. The sensitivity to the proton structure function is low due to the cut in p_T which restricts the range of Bjorken x to $x_{Bj} > 0.03$.

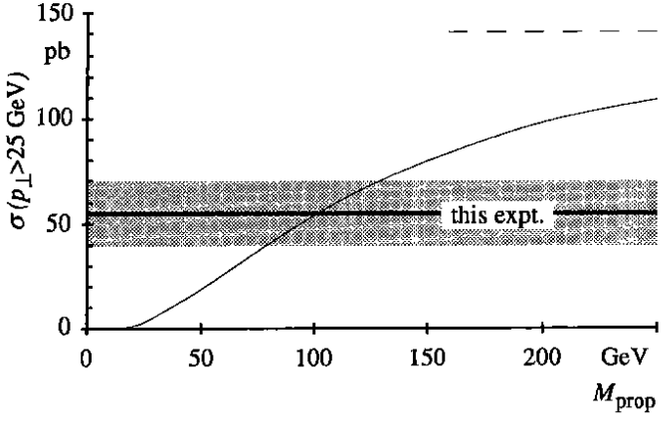

Figure 27: *The CC cross section predicted as function of the propagator mass M_{prop} (= M_W, thin solid line). The dashed line indicates the asymptotic case $M_W \to \infty$. The shaded area represents the 1σ band of the measured cross section.*

Figure 27 shows the sensitivity of the predicted cross section to the mass M_W of the exchanged gauge boson due to the term $1/(1 + Q^2/{M_W}^2)^2$. The value for the propagator mass inferred from this measurement agrees well with the known W mass of 80.2 GeV and excludes the asymptotic case $M_W \to \infty$. Owing to the high center-of-mass energy provided by HERA, the effect of the finite mass of the W in deep inelastic charged current interactions is visible here for the first time.

6 Search for New Particles

HERA offers the attractive possiblity to continue the direct searches for new ("exotic") particles up to masses around 300 GeV. There are two types of particle formation for which HERA is particularly well suited (see fig. 28): This is the production of leptoquarks and leptogluons, where the incoming electron and quark (gluon) fuse to an intermediate state, and the production of excited leptons (heavy electrons or neutrinos), which are formed in the fusion of the incoming electron and the exchanged gauge boson. Another interesting class of new particles is expected by supersymmetry in its R-parity violating variant. Comprehensive reviews on the physics beyond the standard model can be found elsewhere.[91]

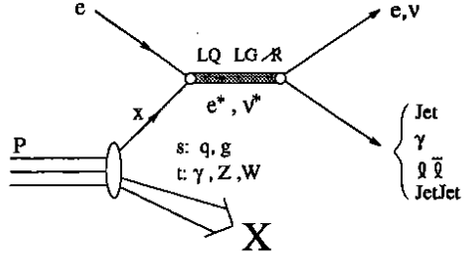

Figure 28: *Born term diagram for the formation of resonances such as leptoquarks, excited leptons, supersymmetric particles etc.*

In the narrow width approximation the cross section for the production of exotic particles E with mass M in ep collisions at a centre-of-mass energy $\sqrt{s}$ can be generally expressed as

$$\sigma(ep \to E + X) = \frac{4\pi^2}{s}(2J+1)\frac{\Gamma}{M}B f_{i/p}\left(\frac{M^2}{s}\right), \qquad (19)$$

where J is the spin of the exotic particle and B its branching ratio into a specific final state. $f_{i/p}$ is a number density of constiutents (quarks or gauge bosons, forming the exotic state together with the incoming electron) radiated off the proton. The width Γ contains all the specific couplings of the exotic particles to the particles in the initial state. Any production of such new heavy states will result in anomalous high Q^2 events at "fixed" Bjorken x, compared to the standard deep inelastic scattering. No such signals have been found yet by H1,[92] based on the luminosity accumulated in 1992.

As specific examples we first discuss the production of excited electrons and neutrinos which are expected in composite models of the known fermions. Assum-

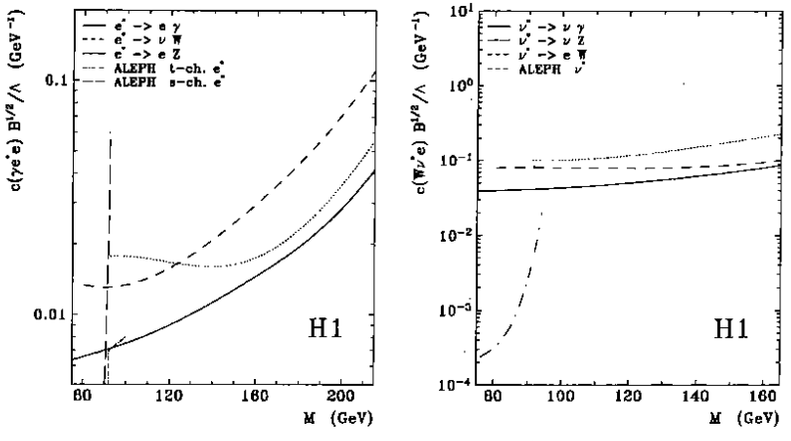

Figure 29: *Rejection limits for the quantity $c_{Vl^*l}\sqrt{B}/\Lambda$ (see text) for excited electrons and neutrinos as function of the e^* (ν^*) mass.*

ing a magnetic-type coupling, the width Γ, introduced in eqn. (19), is given by $\Gamma = \alpha M^3 c^2_{Vl^*l}/\Lambda^2$, where c_{Vl^*l} is a coupling coefficient of a gauge boson V (γ or W, Z^0) to the electron and the excited state (e^* or ν^*), and Λ is the compositeness scale. The current rejection limits from the LEP experiments[94] exclude masses ≤ 90 GeV for $\Lambda \leq 2.5$ TeV. With HERA, masses up to 296 GeV are accessible in principle. Figure 29 shows the rejection limits from the 1992 running period[93] for e^* and ν^* production and decay into photons and heavy gauge bosons. These limits improve our previous measurements[92] by combining the various decay channels of the W and Z^0 (leptonic and hadronic decays).

Leptoquarks are postulated in almost any model beyond the standard theory with the aim to establish a connection between the lepton and quark generations. For leptoquark production, a unique physics reaction for HERA, the coupling Γ is given by $\gamma = (\lambda^2/n\pi)M$, where $n = 16$ for scalar (S) and $n = 24$ for vector (V) leptoquarks. M is the mass of the leptoquark with coupling λ to the lepton-quark pair. Limits for leptoquark production, based on the luminosity accumulated in 1992, have been presented earlier.[92] New, preliminary results for leptoquarks beyond the W mass, using the 1993 data † corresponding to an

†This material has not been presented in the 1993 SLAC Summer Institute's Topical Conference.

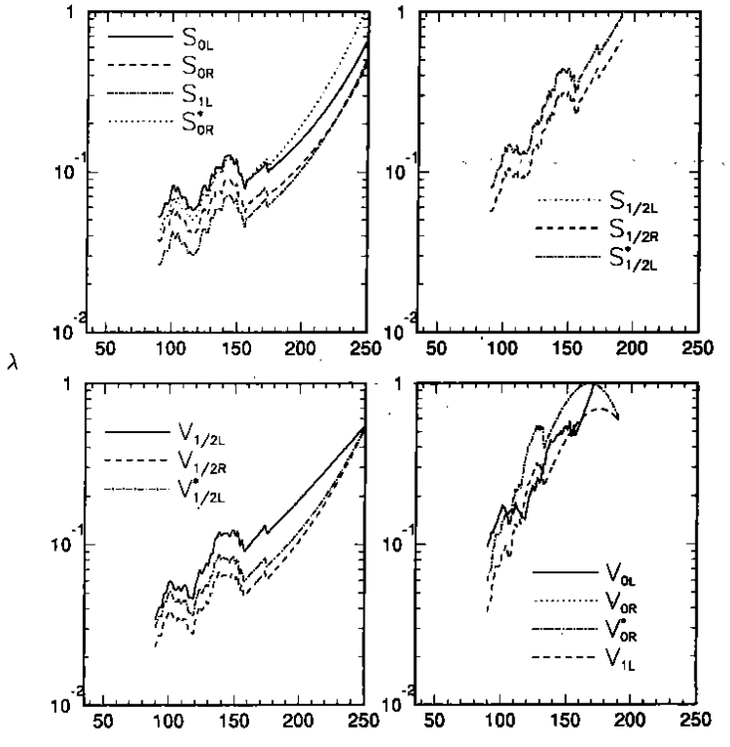

Figure 30: *Rejection limits for the coupling constant λ, for leptoquark production as function of the leptoquark mass.*

integrated luminosity of about 350 nb^{-1} , are shown in fig. 30. The left two parts of the figure give the limits for leptoquark formation of electrons on valence quarks in the various possible spin and weak charge combinations (see[95] for details on the nomenclature), while the right parts give the limits for production on sea antiquarks. Clearly, the latter limits are weaker due to the suppressed momentum fraction carried by the sea quarks. The limits are derived on the assumption that all observed events with jets and electrons (neutrinos) in the final state are explained by standard deep inelastic production. No signal is found in the accessible mass range up to 250 GeV.

7 Conclusions

The first year of luminosity at HERA was quite successful for the H1 experiment. A large number of interesting, and in some cases surprising, physics results have been obtained with still modest statistics, showing the great physics potential of the detector. Among these are the clear observation of jets in photoproduction, equally clear indications of the partonic structure of the photon, and the measurement of the total photoproduction cross section, excluding the class of extreme minijet models inferred from cosmic ray experiments. Measurements of deep inelastic scattering show a steep rise of the proton structure function towards low x, which will be very interesting to follow with more statistics. Analyses of the jet rates seem to indicate a running α_s, and events with a large rapidity gap, indicative of hard diffraction scattering, have been observed.

In 1993 the total integrated luminosity was increased by a factor of twenty and physics analyses on these data are in progress. As an example, a first measurement of the charged current cross section could be presented and limits of particle production beyond the standard model show the high sensitivity of the H1 experiment. H1 is eagerly waiting for more luminosity to come.

Acknowledgements

This work would have been impossible without the immense efforts of all the physicists, engineers and technicians of the H1 Collaboration, who made this experiment a success. I am particularly grateful to my collegues J. Feltesse and A. De Roeck for a critical reading of the manuscript and many helpful suggestions. I profitted a lot from discussions with J. Dainton. The assistence of A. Gruber, Ch. Leverenz, J. Moeck and E. Schuhmann is gratefully acknowledged. Last not least I would like to thank the organizers of the SLAC Summer Institute for the very stimulating and most pleasant atmosphere.

References

[1] M. Breidenbach et al., Phys. Rev. Lett. 23 (1969) 935.

[2] For a review see, e.g., J. Feltesse, Proceedings of the Lepton Photon Conference 1989, SLAC, ed. M. Riordan, (1989) 13 and references therein.

[3] P. Amaudruz et al., NMC Collaboration, Phys. Lett. 295B (1992) 159.

[4] B. Wiik, Contribution to the IEEE Particle Accelerator Conference, San Francisco, 1991, DESY HERA report 91-10 (1991);
F. Degele, Contribution to the 3rd International Particle Accelerator Conference, Berlin, 1992, DESY HERA report 92-12 (1992);
Contributions to the XVth International Conference on High Energy Accelerators, Hamburg, 1992, DESY HERA report 92-19 (1992);
and references cited therein

[5] E. Rutherford, Phil. Mag. Vol. 21 (1911) 669; R. Hofstadter, Electron Scattering, New York, Benjamin (1963).

[6] G. Ingelman, P.Schlein, Phys. Lett. 152B (1985) 256

[7] J. D. Bjorken, these proceedings

[8] L. V. Gribov, E. M. Levin and M. G. Ryskin, Nucl. Phys. B188 (1981) 555; Phys. Rep. 100 (1982) 1

[9] A. H. Mueller, Nucl. Phys. B307 (1988) 34; Nucl. Phys. B317 (1989) 573; Nucl. Phys. B335 (1991) 115

[10] for a review on low x physics see J. Bartels and J. Feltesse, Proc. HERA Workshop, DESY, Hamburg (1992), Vol. 1, p. 133, and references therein

[11] G. A. Schuler, Proc. HERA Workshop, DESY, Hamburg (1992), Vol. 1, p. 461, and references therein

[12] W. Buchmüller, D. Haidt, W. Hollik, Proc. HERA Workshop, DESY, Hamburg (1992), Vol. 2, p. 919, and references therein

[13] Ch. Berger, N. Harnew, F. Schrempp, P. M. Zerwas, Proc. HERA Workshop, DESY, Hamburg (1992), Vol. 2, p. 1027, and references therein

[14] A. De Roeck, Invited Talk at the International Europhysics Conference on high Energy Physics, Marseille, July 1993, DESY 94-005

[15] J. Dainton, Invited Talk at the XVI International Symposium on Lepton-Photon Interactions, Cornell, August 1993.

[16] A rather comprehensive account of the first physics results from HERA has been published by G. Wolf, DESY report 92-190 (1992)

[17] A.Blondel and F.Jacquet, Proceedings of the Study of an *ep* Facility for Europe, ed. U.Amaldi, DESY 79/48 (1979) 391

[18] H1 Collaboration, Technical Proposal, Hamburg 1986; DESY report 93-103, July 1993

[19] W. Braunschweig et al., H1 Collaboration, Nucl. Instr. and Meth. A265 (1988) 419, A275 (1989) 246; H1 Calorimeter Group, B. Andrieu et al., DESY 93-047, subm. to Nucl. Instr. and Meth.

[20] T.Ahmed et al., H1 Collaboration, Phys. Lett. B299 (1993) 374

[21] C. Kiesling et al., "Concept for a fast second level trigger using a neural network architecture for the H1 experiment at HERA", Proceedings of the 3rd International Workshop on Software Engineering, Artificial Intelligence and Expert Systems in Nuclear and High energy Physics, Oberammergau, Germany, 1993

[22] J. C. Bizot et al., Hardware study for a topological level 2 trigger, H1-report 09/92-240, DESY, Hamburg (1992); J. C. Bizot et al., Status of simulation for a topological level2 trigger, H1-Report 09/92-212, DESY, Hamburg (1992), unpublished

[23] D. Haidt and H. Pietschmann in: Landolt-Börnstein New Series I/10, Springer (1988)

[24] G. A. Schuler and T. Sjöstrand, Phys. Lett. B300 (1993) 169

[25] J. J. Sakurai, Ann. Phys. 11 (1960) 1 ; M. Gell-Mann and F. Zachariasen, Phys. Rev. 124 (1961) 953 ; Y. Nambu and J. J. Sakurai, Phys. Rev. Lett. 8 (1962) 79

[26] D. O. Caldwell et al., Phys. Rev. Lett. 40 (1978) 1222

[27] G. Yodt, Nucl. Phys. B (Proc. Suppl.) 12 (1990) 277

[28] M. Drees and F. Halzen, Phys. Rev. Lett. 61 (1988) 275; R. Gandhi et al., Phys. Rev. D42 (1990) 263

[29] J. C. Collins and G.A. Ladinsky, Phys. Rev. D43 (1991) 2847; J. R. Forshaw and J. K. Storrow. Phys. Lett. B268 (1991) 116 ; R. S. Fletcher, T. K. Gaisser and F. Halzen, Phys.Rev. D45 (1992) 377

[30] G. A. Schuler and J. Terron, Proc. HERA Workshop, DESY, Hamburg (1992), Vol. 1, p. 599

[31] A. Donnachie and P. V. Landshoff, CERN-TH 6635/92 (1992)

[32] C. F. Weizsäcker, Z. Phys. 88 (1934) 612; E. J. Williams, Phys. Rev. 45 (1934) 729

[33] R. Ross and L. Stodolsky, Phys. Rev. 149 (1966) 1172

[34] S. Levonian, Proc. HERA Workshop, DESY, Hamburg (1992), Vol. 1, p. 499

[35] H. Abramowicz et al., Phys. Lett. B269 (1991) 465

[36] M. Drees and K. Grassie, Z. Phys. C28 (1985) 451

[37] M. Derrick et al., ZEUS Collaboration, Phys. Lett. B293 (1992) 465

[38] S. Levonian, Low and Medium p_T photoproduction at HERA, Proc. Moriond Conference on QCD, Les Arcs, March 1993

[39] T. Ahmed et al., H1 Collaboration, Phys. Lett. B297 (1992) 205

[40] M. Derrick et al., ZEUS Collaboration, Phys. Lett. B293 (1992) 465

[41] W. Stirling and Z. Kunszt, Proc. HERA Workshop, DESY, Hamburg (1987), Vol. 1, p.331

[42] I. Abt et al., H1 Collaboration, DESY 94-030, March 1994

[43] H.-U. Bengtsson and T. Sjöstrand, Comm. Phys. Comm. 46 (1987) 43

[44] N.H. Brook, A. DeRoeck and A.T. Doyle, Proc. HERA Workshop, DESY, Hamburg (1992), Vol. 3, p. 1405

[45] J. Morfin and W. K. Tung, Z. Phys. C52 (1991) 13

[46] F.M. Borzumati, B. A. Kniehl, G. Kramer, DESY preprint 93-034 (1993)

[47] C. Albajar et al., UA1 Collaboration, Nucl. Phys. B335 (1990) 261

[48] R. Tanaka et al., AMY Collaboration, Phys. Lett. B277 (1992) 215

[49] J. E. Huth et al., Fermilab-Conf-90/249-E (1990)

[50] A. C. Benevenuti et al., BCDMS Collaboration, Phys. Lett. B 223 (1989) 485

[51] M. Glück, E. Reya and A. Vogt, Z. Phys. C 53 (1992) 127; Phys. Lett. B306 (1993) 391

[52] M. Glück, E. Reya and A. Vogt, Phys. Rev. D46 (1992) 1973

[53] H. Abramowicz, K. Charchula and A. Levy, Phys. Lett. B269 (1991) 458

[54] L.W. Whitlow et al., reanalysis of the SLAC/MIT data, Phys. Lett. B250 (1990) 193

[55] For a review see, e.g., S.R. Mishra and F. Sciulli, Ann. Rev. Nucl. Part. Sci., 39 (1989) 259

[56] Yu. L. Dokshitzer, JETP 46 (1977) 641; V. N. Gribov and L. N. Lipatov, Sov. Journ. Nucl. Phys. 15 (1972) 438, 675; G. Altarelli and G. Parisi, Nucl. Phys. 126 (1977) 297

[57] E. A. Kuraev, L. N. Lipatov and V. S. Fadin, Sov. Phys. JETP 44 (1976) 443 ; ibid 45 (1977) 199

[58] A. D. Martin, W. J. Stirling and R. G. Roberts, Phys. Lett. B 306 (1993) 145, ibid. B 309 (1993) 492

[59] A. Donnachie and P. Landshoff, M/C-th 93/11, DAMTP 93-23

[60] J. Botts et al., Phys. Lett. B304 (1993) 159

[61] T. Ahmed et al., H1 Collaboration, Phys. Lett. B 298 (1992) 469

[62] I. Abt et al., H1 Collaboration, Nucl. Phys. B 407 (1993) 515

[63] I. Abt et al., H1 Collaboration, Z. Phys. C 61 (1994) 59

[64] G. Ingelman, program manual LEPTO 5.2, unpublished; H. Bengtsson, G. Ingelman and T. Sjöstrand, Nucl. Phys. B 301 (1988) 554

[65] K.C. Hoeger, Proc. HERA Workshop, DESY, Hamburg (1992), Vol. 1, p. 43

[66] G. Altarelli and G. Martinelli, Phys. Lett. B76 (1978) 89

[67] J.Blümlein, Phys. Lett. B271 (1991) 267; A.Akhundov et al., Proc. HERA Workshop, DESY, Hamburg (1992), Vol. 3, p. 1285

[68] A. Kwiatkowski, H. Spiesberger and H.-J. Möhring, Comp. Phys. Comm. 69 (1992) 155

[69] W. Placzek, Proc. HERA Workshop, DESY, Hamburg (1992), Vol. 3, p. 1433

[70] M. Derrick et al., ZEUS Collaboration, Phys. Lett. B316 (1993) 412

[71] A. De Rujula et al., Phys. Rev. D10 (1974) 1649

[72] K. Prytz, Phys. Lett. B311 (1993) 286

[73] A.M. Cooper-Sarkar et al., Z. Phys. C39 (1988) 281

[74] I. Abt et al., H1 Collaboration, DESY 93-146, October 1993

[75] J. Martin, ZEUS Collaboration, Proc. Int. Lepton-Photon Symp., Cornell, USA (1993)

[76] S. Bentvelsen, J. Engelen and P. Kooijman, Proc. HERA Workshop, DESY, Hamburg (1992), Vol. 1, p. 23

[77] G. Ingelman, Proc. HERA Workshop, DESY, Hamburg (1992), Vol. 3, p. 1366

[78] L. Lönnblad, ARIADNE version 4.03, Comp. Phys. Comm. 71 (1992) 15 and references therein

[79] G. Marchesini, B.R. Webber et al., Comp. Phys. Comm. 67 (1992) 465

[80] T. Sjöstrand, Comp. Phys. Comm. 39 (1986) 347; T. Sjöstrand and M. Bengtsson, Comp. Phys. Comm. 43 (1987) 367; T. Sjöstrand, CERN-TH-6488-92 (1992)

[81] I. Abt et al., H1 Collaboration, DESY 94-033, March 1994

[82] M. Arneodo et al., EMC Collaboration, Z. Phys. C35 (1987) 417

[83] D. Graudenz, Phys. Lett. B 256 (1991) 518, preprint LBL-34147 (1993); T. Brodkorb, J. G. Körner, Z. Phys. C54 (1992) 519; T. Brodkorb et al., Z. Phys. C44 (1989) 415; F.A. Berends, W.T. Giele and H. Kuijf, Nucl. Phys. B231 (1989) 39; K. Hagiwara and D. Zeppenfeld, Nucl .Phys. B313 (1989) 560

[84] W. Bartel et al., JADE Collaboration, Z. Phys. C33 (1986) 23

[85] M. Derrick et al., ZEUS Collaboration, Phys. Lett. B315 (1993) 481

[86] K. Goulianos, Phys. Rep. 101 (1983) 169

[87] P. Bruni, G. Ingelman, A. Solano, Proc. HERA Workshop, DESY, Hamburg (1992), Vol. 1, p. 363

[88] H. Jung, RAPGAP generator, DESY 93-182 (1993)

[89] T. Ahmed et al., H1 Collaboration, Phys. Lett. B324 (1994) 241

[90] H. Spiesberger, EPRC91, unpublished program manual, 1991; Nucl. Phys. B349 (1991) 109; preprint BI-TP 93/03, Jan. 1993

[91] see, e.g., Ch. Berger, N. Harnew, F. Schrempp, P. Zerwas, Proc. HERA Workshop, DESY, Hamburg (1992), Vol. 2, p. 1027, and references therein

[92] I. Abt et al., H1 Collaboration, Nucl. Phys. B396 (1993) 3

[93] F. Raupach, *Search for leptoquarks, leptogluons, excited leptons and squarks in H1 at HERA*, Proc. of the International Europhysics Conference on High Energy Physics, Marseille, July 1993

[94] D. Decamp et al., ALEPH Coll., Phys. Rep. 216 (1992) 253; O. Adriani et al., L3 Coll., Phys. Lett. B288 (1992) 404; B. Adeva et al., L3 Coll., Phys. Lett. B252 (1990) 525; M. Z. Akrawy et al., OPAL Coll., Phys. Lett. B257 (1991) 531, B244 (1990) 135; P. Abreu et al., DELPHI Coll., Z. Phys. C53 (1992) 41, Phys. Lett. B268 (1991) 296

[95] F. Schrempp, Proc. HERA Workshop, DESY, Hamburg (1992), Vol. 2, p. 1034